arXiv:astro-ph/0211194 v2 2 Apr 2003

SHOCK BREAKOUT IN CORE-COLLAPSE SUPERNOVAE AND ITS NEUTRINO SIGNATURE

TODD A. THOMPSON[1]

Astronomy Department and Theoretical Astrophysics Center, 601 Campbell Hall,
The University of California, Berkeley, CA 94720; thomp@astro.berkeley.edu

ADAM BURROWS

Steward Observatory, The University of Arizona, Tucson, AZ 85721; burrows@zenith.as.arizona.edu

PHILIP A. PINTO

Steward Observatory, The University of Arizona, Tucson, AZ 85721; ppinto@as.arizona.edu

ABSTRACT

We present results from dynamical models of core-collapse supernovae in one spatial dimension, employing a newly-developed Boltzmann neutrino radiation transport algorithm, coupled to Newtonian Lagrangean hydrodynamics and a consistent high-density nuclear equation of state. The transport method is multi-group, employs the Feautrier technique, uses the tangent-ray approach to resolve angles, is implicit in time, and is second-order accurate in space. We focus on shock breakout and follow the dynamical evolution of the cores of $11\,M_\odot$, $15\,M_\odot$, and $20\,M_\odot$ progenitors through collapse and the first 250 milliseconds after bounce. The shock breakout burst is the signal event in core-collapse evolution, is the brightest phenomenon in astrophysics, and is largely responsible for the initial debilitation and stagnation of the bounce shock. As such, its detection and characterization could test fundamental aspects of the current collapse/supernova paradigm. We examine the effects on the emergent neutrino spectra, light curves, and mix of species (particularly in the early post-bounce epoch) of artificial opacity changes, the number of energy groups, the weak magnetism/recoil corrections, nucleon-nucleon bremsstrahlung, neutrino-electron scattering, and the compressibility of nuclear matter. Furthermore, we present the first high-resolution look at the angular distribution of the neutrino radiation field both in the semi-transparent regime and at large radii and explore the accuracy with which our tangent-ray method tracks the free propagation of a pulse of radiation in a near vacuum. Finally, we fold the emergent neutrino spectra with the efficiencies and detection processes for a selection of modern underground neutrino observatories and argue that the prompt electron-neutrino breakout burst from the next galactic supernova is in principle observable and usefully diagnostic of fundamental collapse/supernova behavior. Though we are not in this study focusing on the supernova mechanism per se, our simulations support the theoretical conclusion (already reached by others) that spherical (1D) supernovae do not explode when good physics and transport methods are employed.

Subject headings: supernovae, neutrinos, radiative transfer, spectra

1. INTRODUCTION

The most dynamical phase of core-collapse supernova evolution is the epoch of core bounce, shock wave formation, and early shock propagation. Within a few milliseconds (ms) of birth, the shock wave propagates down the density gradient from where it is formed at $\sim 10^{14}$ g cm^{-3} and $\sim$10 kilometers to where it dies into an accretion shock at $\sim 10^{10}$ g cm^{-3} and $\sim$100–120 kilometers. Between birth and death, the shock wave, born in the neutrino-opaque region, emerges into the neutrino-transparent region. In the process, it "breaks out" through the neutrinospheres of the various neutrino species (ν_e, $\bar{\nu}_e$, and "ν_μ"s), and, thereby, produces an ultra-luminous burst of neutrinos brighter than any other phenomenon in astrophysics. This short transient is responsible for sapping the shock of energy and aborting the supernova explosion within 10-20 ms of its birth and is a primary reason the supernova the-

orist has shifted focus to the "long-term" mechanism of shock revival in its various forms (Bethe & Wilson 1985; Herant et al. 1994; Burrows, Hayes, & Fryxell 1995; Fryer et al. 1999; Fryer & Heger 2000; Rampp & Janka 2000; Janka 2001; Liebendörfer et al. 2001; Liebendörfer, Mezzacappa, & Thielemann 2001).

Given the central importance of the breakout phenomenon to the dynamics of core collapse (as we think we understand it), and given the possibility that the next galactic supernova will be detected by neutrino telescopes far more sensitive than the underground detectors IMB and Kamioka II which caught SN1987A, we have made a detailed study of the breakout phenomenon, its neutrino signature, and its dependence on various parameters, progenitors, and neutrino microphysics. Neutrino breakout is the signature characteristic of the theory of collapse and supernovae, that if measured would speak volumes concerning the dynamics of a dense core otherwise obscured from

[1] Hubble Fellow

view.

In §2, we describe our multi-group, multi-angle radiation/hydrodynamics code SESAME[2] and the microphysics we use in this survey of the breakout phenomenon. We include a discussion of our implementation of the Lattimer-Swesty high-density nuclear equation of state (LSEOS) in Appendix A. In §3, we present our baseline core-collapse simulation using an $11\,M_\odot$ progenitor from Woosley & Weaver (1995). We follow the discussion of this reference model with studies of the dependence on spectral resolution (§4), progenitor mass (§5), the nuclear equation of state (§6), the weak magnetism/recoil correction (§7.2), and the role of nucleon-nucleon bremsstrahlung (§7.3). In §7.4, using a new explicit algorithm for handling it (see Appendix B), we explore the effect of inelastic neutrino-electron scattering. In §8, event rates and signatures in the underground telescopes Super Kamiokande, SNO, and ICARUS are calculated and described. It is shown that the breakout burst is in principle detectable in all three of these neutrino observatories. Changes in the observed neutrino signal due to modifications in the microphysics employed in the simulations are also presented. We wrap up in §9 with a summary and general conclusions on the breakout phenomenon and its model dependencies. Our focus in this paper is on the breakout phenomenon, not the supernova itself. Hence, our simulations are restricted (for the most part) to the first 250 ms after bounce.

2. NUMERICAL METHODS

2.1. *Radiation Transport*

The mass densities, temperatures, and compositions that obtain during core collapse conspire to produce regions in the deep core of a supernova where the mean-free-path for neutrinos is just meters and the transport could be handled using simple diffusion theory. Simultaneously, there are regions at larger radius where each neutrino species decouples from the matter and free-streams to infinity. In between, at modest optical depth, where the neutrino mean-free path is a modest fraction of the size of the object as a whole, the full transport problem must be solved in order to obtain accurate values of the local neutrino flux and energy density - both critical in determining the energy deposition profile and, hence, the subsequent evolution.

Our Boltzmann transport solver (Burrows et al. 2000) is due primarily to Eastman & Pinto (1993), who developed an algorithm for solving the comoving transport equation using the Feautrier variables and the tangent-ray method for angular discretization. The transport solver is implicit in time and second-order accurate in space. The zeroth- and first-moment equations are iterated with the Boltzmann/transport equation using Accelerated Lambda Iteration (ALI) to speed convergence of the radiative transfer solution (see e.g., Mihalas & Mihalas 1984). Only the diagonal and the adjacent off-diagonal terms of the Λ matrix are used. This method is akin to the standard variable Eddington factor (VEF) approach, but no ad hoc flux limiters or artificial closures are necessary. The iteration scheme generally converges to a part in 10^6 in 2 to 10 steps, and automatically conserves energy in the transport sector. The Feautrier scheme can transition to the diffusion limit seamlessly and accurately and the tangent-ray method automatically adapts with the Lagrangean hydrodynamic grid as it moves. In constructing the

tangent rays, we cast them from every outer zone to every inner zone. Hence, if there are 300 radial zones, the outer zone has 299 angular groups in each quadrant of the unit circle. Because of the spherical nature of the core-collapse problem and the need to accurately reproduce the angular distribution of the radiation field that transitions from the opaque (inner) to the transparent (outer) regions, such fine angular resolution is useful, though computationally demanding, as radiation becomes more and more forward-peaked.

The coupling of the neutrino radiation to matter is done implicitly in operator-split fashion, using the Accelerated Lambda operator to obtain the derivative '$\partial J / \partial S$' (where S is the source function) after each hydrodynamic update. This derivative is required for the implicit updates of temperature (T) and electron fraction (Y_e) (Burrows et al. 2000).

We solve the transport equation for ν_e neutrinos, $\bar{\nu}_e$ neutrinos, and ν_μ neutrinos, where 'ν_μ' stands for ν_μ, $\bar{\nu}_\mu$, ν_τ, and $\bar{\nu}_\tau$. Although in principle the neutrino microphysics is different between ν_μ, $\bar{\nu}_\mu$, ν_τ, and $\bar{\nu}_\tau$ we make the assumption standard in the field that they can be treated identically. The energy grouping is different for each species. For ν_e neutrinos, $1 \le \varepsilon_{\nu_e}$ (MeV) ≤ 320. For $\bar{\nu}_e$ neutrinos, $1 \le \varepsilon_{\bar{\nu}_e}$ (MeV) ≤ 100. Both are grouped logarithmically. For ν_μ neutrinos, $1 \le \varepsilon_{\nu_\mu}$ (MeV) ≤ 100 with uniform grouping in energy. Our baseline models employ 40 energy groups for each species. In §4, we compare our results with calculations employing just 10 and 20 energy groups. Our standard set of microphysics includes all of the emission/absorption and scattering processes described in Burrows (2001) plus weak-magnetism and recoil modifications to the cross sections for neutrino-nucleon absorption and scattering, as per Horowitz (1997, 2002). In addition, we include inelastic neutrino-electron scattering as described in Appendix B. In our baseline models for this paper we do not include inelastic neutrino-nucleon scattering, but include it only as a purely elastic scattering opacity source.

2.2. *Hydrodynamics*

During most epochs in supernova evolution, the radiation pressure term is negligible. However, during breakout when electron neutrino luminosities approach 10^{54} erg s^{-1} locally, this term can be important. Since there is as yet no natural way in PPM-like hydro codes to include the radiation pressure term in the solution to the Riemann problem, we have opted to couple our transport algorithm to a Newtonian and Lagrangean predictor/corrector hydrodynamics scheme that uses artificial viscosity for shock resolution. During and just after shock breakout, since the neutrinospheres and the regions of spectrum formation are found at 30 to 100 kilometers, general-relativistic effects are small to modest, GM/rc^2 being just 3 to 10%. Nevertheless, particularly at later times, general-relativistic effects can introduce $\sim$10% corrections (Bruenn, De Nisco, & Mezzacappa 2001; Liebendörfer et al. 2001).

In the core at bounce the zone size in our calculations is $\sim$200 meters. The sound speed at nuclear densities approaches $\sim c/3$. Hence, our Courant-limited explicit timestep is $\sim 10^{-6}$ seconds. This implies that to evolve a calculation for $\sim$1 second would require $\sim 10^6$ timesteps. The solution to the transport equation for all species is computationally expensive and on current

---

[2] **S**pherical **E**xplicit/Implicit **S**upernova **A**lgorithm for **M**ulti-Group/Multi-Angle **E**xplosion Simulations

single-processor machines 10^6 timesteps is large. In order to circumvent this problem we sub-cycle the hydrodynamics after shock breakout and stall. After this most dynamical phase is over we take $2-4$ hydro steps per transport step, thus cutting the total computational requirements significantly. Introducing sub-cycling ~ 20 milliseconds after bounce seems to introduce errors of less than 1% in all radiation and hydrodynamic quantities.

For all of our simulations, we employ the tabular equation of state described in Appendix §A.

3. THE BASELINE MODEL RESULTS

We take as a reference model to establish the general context of the study an $11\,M_\odot$ progenitor from Woosley & Weaver (1995). The model employs 300 mass zones out to M = 1.43 $M_\odot$, where M is the interior mass; in this progenitor, at M = 1.43 $M_\odot$, r equals 2500 km. For the simulations presented here, which focus on collapse and the early ($\sim 100-200$ ms) post-bounce evolution, we find this zoning sufficient. In §6, we explore the effects of changes in the nuclear compressibility modulus, but for our baseline model we use $\kappa = 220$ MeV in the LSEOS (Appendix A).

Figure 1 shows velocity v (in cm s^{-1}, upper left panel), $\log_{10}[\rho]$ (in g cm^{-3}, upper right panel), entropy s (in k$_B$ baryon^{-1}, lower left panel), and temperature T (in MeV, lower right panel), as a function of mass coordinate in M$_\odot$ at five snapshots in time in our $11\,M_\odot$ baseline model. Fig. 1 is to be compared with Fig. 2, which shows the electron fraction (Y_e) as a function of mass in the same model. The thin solid line in Figs. 1 and 2 is the initial configuration. The thick solid line is at hydrodynamical bounce (approximately 200 ms after we start the calculation). We generally quote times relative to bounce. Bounce coincides with the core density reaching $\sim 2-3 \times 10^{14}$ g cm^{-3}, where the EOS stiffens dramatically. Note that Y_e in the very core reaches its minimum value *before* bounce. At core densities of $\sim 2 \times 10^{12}$ g cm^{-3} the electron-neutrino outward diffusion speed becomes smaller than the the inward collapse speed and the neutrinos are effectively trapped. Soon afterward, the process primarily responsible for the decrease in Y_e, $e^- p \rightarrow n\nu_e$, is balanced by its inverse and beta equilibrium is achieved (Bruenn 1985; Mezzacappa & Bruenn 1993abc). Although we have included inelastic neutrino-electron scattering in our baseline model, the long dashed line in Fig. 2 shows the bounce Y_e profile if one turns off this equilibration process. Because small changes in the Y_e profile at bounce can affect the shock energetics significantly (Burrows & Lattimer 1983) and because inelastic neutrino-electron scattering affects the approach to beta equilibrium by modifying the neutrino phase space occupancy, inelastic neutrino-electron scattering should be included in a full treatment (Bruenn 1985; Mezzacappa & Bruenn 1993abc). We discuss this process and its effects on breakout more fully in §7.4.

At bounce, a strong sound wave is formed deep in the core, which propagates down the density gradient set up by the infalling outer stellar material. The sound wave steepens into a shock near M$\simeq 0.6$M$_\odot$, just ~ 1 ms after bounce. The dotted line in Fig. 1 shows the shock fully formed and at maximum positive velocity ($\sim 1.9 \times 10^9$ cm s^{-1}). Of course, the shock is associated with the generation of entropy and an increase in temperature, as seen in the lower two panels of Fig. 1. As the

shock moves outward in mass and radius it dissociates nuclei into free nucleons. Although the matter is hot in this region, the electrons are still quite degenerate and the process $e^- p \rightarrow n\nu_e$ builds up a sea of electron neutrinos that are trapped and advected with the matter. Figure 3 shows the luminosity of electron neutrinos as a function of mass and time from bounce all the way through breakout. Although the shock does not form until M$\simeq 0.6$M$_\odot$, a phase-transition front which liberates free nucleons from nuclei moves in tandem with the sound wave generated at bounce. This causes the initial luminosity peak seen in Fig. 3 at M$\simeq 0.5$M$_\odot$, or, in this model, at a radius of just 11 km (labeled 'Initial rise due to phase transition'). The sudden drop in L_{ν_e} at M$\simeq 0.6-0.7$M$_\odot$ comes from a sharp decrease in X_p, coincidentally nearly simultaneous with shock formation. Just as the shock is forming, but before the temperature rises dramatically, as shown in the lower right panel of Fig. 1 (dotted line), a region of heavy nuclei exists and, due to the fact that the absorption cross section is not continuous across the phase transition, there is a decrease in L_{ν_e} at M$\simeq 0.6-0.7$M$_\odot$. In Fig. 3, the specific snapshots in time between the 1 ms (dotted) line and the 17 ms (short dashed) line in Figs. 1 and 2 are labeled. At 2.4 ms after bounce the spike reaches a local maximum at M$\simeq 0.85$M$_\odot$, with L_{ν_e} exceeding 1.4×10^{54} erg s^{-1}. This spike roughly denotes the position of the shock. It is at this moment that the shock crosses the ν_e neutrinosphere (R_{ν_e}). The neutrinospheric radius (R_ν) for any neutrino species of energy ε_ν is set approximately by the following integral criterion:

$$\tau_\nu(R_\nu, \varepsilon_\nu) = \int_{R_\nu}^{\infty} \kappa_\nu(\varepsilon_\nu, r)\rho(r)\,dr = \frac{2}{3}, \qquad (1)$$

where κ_ν is the total opacity. At just 3.2 ms after bounce, one can see clearly that the breakout pulse of electron neutrinos is beginning to move ahead of the shock. Having moved into a region where the optical depth is below $\sim 2/3$, the neutrinos begin to free-stream.

The decoupling of the radiation during breakout is perhaps better seen in Fig. 4, which shows the temperature profile (dashed line) with the ν_e luminosity 3.2 ms after bounce (compare with Fig. 3). The four insets (thin solid lines on dotted axes) show polar plots of the specific intensity, $I_{\nu_e}(\theta)$, for $\varepsilon_{\nu_e} = 12$ MeV. The large dots on the temperature profile show the position, in units of enclosed mass, at which the specific intensity has been sampled. At point 'A' ($M \simeq 0.674\,M_\odot$, $r \simeq 21.8$ km), $I_{\nu_e}(\theta)$ is virtually a circle, indicating that the radiation field is isotropic, that the net flux is nearly zero, and that the neutrinos at that position and energy are trapped. In contrast, at point 'D' ($M \simeq 1.03\,M_\odot$, $r \simeq 124.0$ km), $I_{\nu_e}(\theta)$ is very forward-peaked and well-resolved by our tangent-ray algorithm with 160 angles in each quadrant of the unit circle. Insets 'B' and 'C' show $I_{\nu_e}(\theta)$ at intermediate positions, on either side of the shock. The small increases in $I_{\nu_e}(\theta)$ in the forward quadrants of 'C' are consistent with limb-brightening effects from the shock, never before resolved.

Figure 3 shows a marked decrease in the breakout ν_e luminosity pulse just as it begins to propagate ahead of the shock, between the lines labeled 't=2.4 ms' and 't=6.8 ms'. The local maximum of L_{ν_e} at 2.4 ms occurs at a radius of approximately $r_{\rm peak} \simeq 41$ km. We expect the peak luminosity ($L_{\nu_e}^{\rm peak}$) to be attenuated approximately by an amount $\sim \exp(-\tau_a)$ in propagating to infinity ($L_{\nu_e}^\infty$), where τ_a is the total absorptive optical depth exterior to $r_{\rm peak}$. >From the results presented here, we find $\tau_a(r_{\rm peak}) \sim 1.9$ at $\varepsilon_{\nu_e} \simeq 12$ MeV. This simple estimate

shows that we should expect $L_{\nu_e}^{\text{peak}}$ to decay by $\sim 85\%$. With $L_{\nu_e}^{\text{peak}} \simeq 1.45 \times 10^{54}$ erg s^{-1} we expect $L_{\nu_e}^{\infty} \sim 0.22 \times 10^{54}$ erg s^{-1} and find from the simulation that $L_{\nu_e}^{\infty} \simeq 0.25 \times 10^{54}$ erg s^{-1}, in good agreement with our estimate. This asymptotic luminosity is shown clearly as the bump in the last line in Fig. 3, labeled 'Breakout Pulse', which has moved out to $1.35\,\text{M}_\odot$. Behind the pulse, at M$\simeq 1.08\,\text{M}_\odot$, is a sharper peak in the luminosity that denotes the shock position. During this breakout phase of shock evolution, much of the shock energy is sapped by the neutrino losses that attend electron capture on newly-liberated free protons. This process also creates a characteristic deleptonization trough manifest by the marked decrease in Y_e in Fig. 2 near M$\simeq 0.8\,\text{M}_\odot$. The shock stalls quickly and in just a few milliseconds after bounce all velocities are ≤ 0. Note the negative entropy gradient between M$\simeq 0.75\,\text{M}_\odot$ and M$\simeq 0.95\,\text{M}_\odot$. Depending upon the compositional gradients in this region, in a multi-dimensional simulation this region might be convectively unstable (Burrows and Fryxell 1992; Keil, Janka, and Müller 1996).

Although the shock continues to move outward in mass as matter flows through it from the free-falling outer core, all matter velocities are negative by the time the shock reaches $r \sim 80 - 90\,\text{km}$. The short dashed lines in Figs. 1 and 2 show the configuration of the model 17 ms after bounce and ~ 10 ms after the shock has stalled. The dot-dashed line shows these basic hydrodynamical quantities 200 ms post-bounce. The shock has consumed another $0.2\,\text{M}_\odot$ of infalling material and the entropy behind the shock has increased dramatically. The temperature over the whole post-shock profile has increased as a result of the compressional work done on these zones by the infalling stellar material. In particular, at the peak in the temperature profile at M$\sim 0.7\,\text{M}_\odot$, T increased by ~ 4 MeV between $t = 17$ ms and $t = 200$ ms. In these hundreds of milliseconds after bounce, the shock moves outward in radius to ~ 175 km. Although it is in this epoch that neutrino heating behind the shock is thought to revive it, no explosion is seen in our simulations at this time. Figure 5 shows the evolution of selected mass zones in our $11\,\text{M}_\odot$ model as a function of time. Small oscillations are visible just after bounce - the 'ringing' of the core - and the shock position is made clear by the change in the infalling matter velocity between 100 km and 200 km during the 280 ms of post-bounce evolution shown here. Although the neutrino-driven mechanism is not the focus of this work, from this figure and from many similar calculations we see no evidence of explosion.

In Fig. 3, we showed L_{ν_e} as a function of mass at various snapshots in time. The last snapshot shows the ν_e breakout pulse at $1.35\text{M}_\odot$ and propagating at the speed of light to the edge of the grid. Complementary to Fig. 3, the time evolution of L_{ν_e} at infinity is shown in Fig. 6 (thick solid line). The luminosity of anti-electron neutrinos ($L_{\bar{\nu}_e}$, thin solid line) and the combined luminosity of ν_μ, $\bar{\nu}_\mu$, ν_τ, and $\bar{\nu}_\tau$ (collectively, L_{ν_μ}, dotted line) are also shown for the first 250 ms of post-bounce evolution. Note that just before the major breakout pulse of electron neutrinos, there is another small peak that reaches $\sim 0.72 \times 10^{53}$ erg s^{-1}. This peak results from the deleptonization of the core as the Y_e drops in Fig. 2 from that of the initial model to $Y_e \simeq 0.27$. There is a small dip in L_{ν_e} just after this initial rise. This dip in the asymptotic luminosity signals the end of the infall/collapse phase of the supernova. After the initial increase in L_{ν_e} due to deleptonization, L_{ν_e} decreases because of the increased opacity

in the dense collapsing core. The high opacity decreases the local luminosity at small radii and isolates the precursor peak in luminosity at larger radii caused by early deleptonization. If it were not for shock formation, L_{ν_e} at infinity would continue to decline. The main breakout pulse just after the small downturn in L_{ν_e} results from the dissociation of nuclei and subsequent electron capture on free protons, as described above and shown in Fig. 3.

In Fig. 7 we show the corresponding average neutrino energy for each species over the same time interval as Fig. 6. There are many ways one might define the average neutrino energy. The literature does not consistently employ a unique prescription and considerable confusion exists. The average energy we present in our figures is the *rms* average energy, defined by:

$$\langle \varepsilon_\nu \rangle = \left[\frac{\int d\varepsilon_\nu \varepsilon_\nu^2 J_\nu(\varepsilon_\nu)}{\int d\varepsilon_\nu J_\nu(\varepsilon_\nu)} \right]^{1/2}, \qquad (2)$$

where $J_\nu(\varepsilon_\nu)$ is the zeroth moment of the specific intensity. We use this definition in order to make comparisons with other recent work (Liebendörfer et al. 2001; Rampp et al. 2002). After approximately 50 ms, the average energies show a nearly linear increase with time. Mezzacappa et al. (2001) and Liebendörfer et al. (2001) find similar behavior. In addition, although we employ a different progenitor, the values for the average neutrino energies they obtain compare well with those presented in Fig. 7. For example, 250 ms after bounce in their $13\,M_\odot$ progenitor, Mezzacappa et al. (2001) obtain $\langle \varepsilon_{\nu_\mu} \rangle \simeq 21$ MeV, $\langle \varepsilon_{\bar{\nu}_e} \rangle \simeq 16$ MeV, and $\langle \varepsilon_{\nu_e} \rangle \sim 14$ MeV. We find that $\langle \varepsilon_{\nu_\mu} \rangle \simeq 20$ MeV, $\langle \varepsilon_{\bar{\nu}_e} \rangle \simeq 15.5$ MeV, and $\langle \varepsilon_{\nu_e} \rangle \sim 13$ MeV.

Figure 8 shows the luminosity spectrum of electron neutrinos at infinity in units of 10^{52} erg s^{-1} MeV^{-1}. The thick solid line denotes the maximum peak breakout pulse luminosity and corresponds to the 2.55×10^{53} erg s^{-1} peak in L_{ν_e} in Fig. 6. The thin solid lines in this plot show the rise up to the peak and the simultaneous shift in $\langle \varepsilon_{\nu_e} \rangle$ depicted in Fig. 7. The dashed lines show the evolution of the luminosity spectrum after the breakout pulse. The pre-breakout lines show the spectrum at 11.6, 5.1, and 1.3 ms before the peak in the breakout pulse. The dashed, post-breakout, lines show the spectrum at 4.2, 9.6, and 40.5 ms after the ν_e breakout pulse. Although in this figure the peak energy is dropping as the luminosity decays, the high energy tail becomes broader and with our definition of the average energy (eq. 2) $\langle \varepsilon_{\nu_e} \rangle$ increases. Figure 9 shows the emergent spectrum much later (at 210 ms after bounce) and for all three neutrino species. The thick solid line shows the ν_e spectrum, the thin solid line shows the $\bar{\nu}_e$ spectrum, and the dotted line shows the combined ν_μ spectrum. The post-bounce energy hierarchy one expects from simple considerations of the opacity sources for the various species, $\langle \varepsilon_{\nu_e} \rangle < \langle \varepsilon_{\bar{\nu}_e} \rangle < \langle \varepsilon_{\nu_\mu} \rangle$, is evident in both Figs. 7 and 9.

Although this exact progenitor model has not been used in any of the recent supernova modeling done by groups employing sophisticated neutrino transport (Rampp 2000; Rampp & Janka 2000, 2002; Liebendörfer et al. 2001; Liebendörfer, Mezzacappa, & Thielemann 2001; Mezzacappa et al. 2001), we find that the basic structures and systematics are similar between groups. In particular, our core entropy (s_{core}) drops slightly at the beginning of the calculation and then climbs during bounce to $s_{\text{core}} \simeq 1.32\,k_B$ baryon^{-1}. We observe similar behavior for our $15\,M_\odot$ progenitor with $s_{\text{core}} \simeq 1.33\,k_B$ baryon^{-1}. Without inelastic neutrino-electron scattering we obtain $s_{\text{core}} \simeq 1.16\,k_B$ baryon^{-1}. The absolute magnitude of these

results and the effect of neutrino-electron scattering on s_{core} are duplicated in the work of Rampp (2000), whose Figs. 5.3a and 5.6b shows that with and without neutrino-electron scattering in their 15 M$_\odot$ model they obtain $s_{core} \simeq 1.3$ and $1.14\,k_B$ baryon^{-1}, respectively. A recent collapse calculation by Liebendörfer et al. (2002b) of a 13 M$_\odot$ progenitor also shows $s_{core} \sim 1.3\,k_B$ baryon^{-1}. Core Y_e (Y_e^{core}) in our 11 M$_\odot$ model drops to 0.266 and 0.293 at bounce in our models with and without neutrino-electron scattering, respectively. Both numbers from Rampp (2000) are slightly higher; his Fig. 5.3b gives the corresponding numbers as approximately 0.28 and $0.30-0.31$, respectively. Liebendörfer et al. (2002b) have $Y_e^{core} \simeq 0.30$, including neutrino-electron scattering. Peak positive velocities in all our calculations reach $\sim 2 \times 10^9$ cm s^{-1} at M$\simeq 0.7$M$_\odot$ - in good agreement with previous work.

One important difference bears mention. Our peak breakout electron-neutrino luminosity is slightly lower than that obtained in other work. Both Liebendörfer et al. (2001) and Rampp & Janka (2000) obtain $L_{\nu_e}^{peak}$ of $\sim 3.5 \times 10^{53}$ erg s^{-1} with comparable progenitors. Indeed, Liebendörfer et al. (2002a) present the breakout pulse for several different progenitors and find virtually identical $L_{\nu_e}^{peak}$ for all models. We obtain $L_{\nu_e}^{peak} \simeq 2.55 \times 10^{53}$ erg s^{-1} in our 11M$_\odot$ and virtually the same number with the 15 M$_\odot$ and 20 M$_\odot$ models we present in §5. Our results consistently give lower $L_{\nu_e}^{peak}$ by about 30%. This luminosity pulse is a signature of the most dynamical phase in supernova modeling and it is important to achieve adequate angular, energy, and spatial zoning to resolve it. For comparison, Mezzacappa et al. (2001) and Liebendörfer et al. (2001) typically employ eight angular bins using the S$_n$ method at each radial point and twelve energy groups. In particular, poor angular resolution at large radii may compromise the propagation of the breakout pulse. Liebendörfer et al. (2002b) state that they experience significant "numerical diffusion" of their breakout pulse as it propagates from the point of decoupling to the edge of their computational grid. The peak asymptotic luminosity they quote, $L_{\nu_e}^{peak} \sim 3.5 \times 10^{53}$ erg s^{-1}, is sampled at 500 km in their calculations. This peak drops $\sim$30% to $\sim 2.25 \times 10^{53}$ erg s^{-1} in propagating to $\sim$4200 km (see their Fig. 14 and Fig. 20). Plotting the radial coordinate of the peak in the luminosity pulse as a function of $r-ct$, Liebendörfer et al. (2002b) find that $L_{\nu_e}^{peak}$ decreases, shifts by $\sim 500-1000$ km, and broadens due to numerical diffusion. Constructing a similar plot with our collapse calculations, over a similar range of radii, we find a shift in the pulse peak of just $\lesssim$10 km, or a fractional deviation from c of $\sim$0.3%. We also find a decrease in $L_{\nu_e}^{peak}$ between 500 km and 4200 km of 8.5%. In short, we obtain a lower asymptotic ν_e breakout pulse than Liebendörfer et al. (2002b), that cannot be explained by the considerable numerical diffusion in their first-order upwind differencing scheme. Using the tangent-ray method, our $L_{\nu_e}^{peak}$ does not experience the same degradation and maintains an on-grid speed remarkably close to c after fully decoupling from the matter.

Although they describe it as diffusion, the temporal dispersion and decay Liebendörfer et al. (2002b) experience in the electron-neutrino breakout pulse might be better interpreted as a consequence of the progressive loss of angular resolution as the luminosity pulse propagates outward and, thereby, becomes more and more forward-peaked. Though a fixed angular grid with eight points can not resolve a sharply-pointed pulse, it

should be adequate for calculating the flux factors of relevance to neutrino energy deposition in the gain region and for gauging the viability of the neutrino mechanism of supernova explosions.

Two hundred milliseconds after bounce, the shock has moved out to about 200 km in radius. A gain region of net heating has formed between the gain radius $R_g \simeq 100$ km (where heating balances cooling) and the shock. For $\varepsilon_{\nu_e} = 10.7$ MeV, the ν_e neutrinosphere (R_{ν_e}, as defined in eq. 1) occurs at $\simeq 60$ km. Between R_{ν_e} and R_g is a region of net cooling. The solution to the Boltzmann equation yields the specific intensity of the neutrino radiation field, I_ν, as a function of both energy and angle, at every radial coordinate and timestep. When neutrinos of a given energy are trapped and diffusive, their radiation field is isotropic in angle. Beyond the neutrinosphere, where they approach the free-streaming limit, the neutrino radiation field becomes continuously more forward-peaked. In an effort to understand the angular distribution of I_{ν_e}, Fig. 10 shows a polar plot of $I_{\nu_e}(\theta)$ for many ν_e energies at $R_{\nu_e}(\varepsilon_{\nu_e} = 10.7\,\text{MeV}) = 60$ km. All curves in this figure have been normalized to the same maximum specific intensity. The outer near-circle (thick solid line) in this figure shows $I_{\nu_e}(\theta)$ for $\varepsilon_{\nu_e} = 320$ MeV. Fig. 10 shows that although 60 km is R_{ν_e} for neutrinos with $\varepsilon_{\nu_e} = 10.7$ MeV, 320 MeV neutrinos are completely trapped at this radius; $I_{\nu_e}(\theta)$ is isotropic and the net flux is nearly zero for $\varepsilon_{\nu_e} = 320$ MeV. This is a consequence of the fact that the neutrino opacity is proportional to ε_ν^2. Also shown is $I_\nu(\theta)$ for other neutrino energies down to 1 MeV (also a thick solid line). Only every other neutrino energy calculated is shown. Going from high to low energies, one sees that the radiation field becomes less isotropic, the lowest energies being the most forward-peaked. The $\varepsilon_{\nu_e} = 10.7$ MeV point is highlighted (middle thick solid line) to show the angular distribution of the radiation field at the neutrinosphere for that energy. A glance at Fig. 10 shows how forward-peaked the radiation field is at the point of decoupling (the neutrinosphere), for a given energy (in this case, 10.7 MeV). Note that in this calculation, R_{ν_e} occurs at our 270th radial zone, so that in each quadrant of the polar plot there are 269 angular bins.

Also of interest is the dependence of the angular distribution of the radiation field on radius for a given energy. Figure 11 shows how $I_{\nu_e}(\theta, \varepsilon_{\nu_e} = 10.7\,\text{MeV})$ evolves from the neutrinosphere radius ($\sim$60 km, outer thick solid line) to the shock radius ($R_s \simeq 200$ km, inner thick solid line). Also shown is $I_{\nu_e}(\theta)$ at R_g, where heating balances cooling, and $I_{\nu_e}(\theta)$ at larger radii, where heating dominates. This figure shows that the angular distribution of the radiation field is quite forward-peaked in the heating region. As noted in Liebendörfer et al. (2002b), insufficient angular resolution in this region can lead to artificial enhancements in the energy deposition profile and, hence, could affect the subsequent dynamics. In Fig. 12, we show the neutrinosphere radius (as defined in eq. 1) as a function of energy for all neutrino species at four different snapshots in time from just after breakout to 200 ms after bounce. R_{ν_e}, $R_{\bar{\nu}_e}$, and R_{ν_μ} are the thick, thin, and dotted lines, respectively. The break in the neutrinosphere radius profiles at approximately 50 km, 70 km, and 100 km in the first three panels roughly denotes the position of the shock. The bottom-right panel corresponds roughly in time with the polar plots of the radiation field in Figs. 10 and 11. Note that the energy hierarchy, $\langle \varepsilon_{\nu_e} \rangle < \langle \varepsilon_{\bar{\nu}_e} \rangle < \langle \varepsilon_{\nu_\mu} \rangle$, is reflected here: $R_{\nu_\mu} < R_{\bar{\nu}_e} < R_{\nu_e}$.

4. SPECTRAL RESOLUTION

Our baseline model employs 40 energy groups for each neutrino species, with the actual grouping described in §3. In an effort to understand the effects of degrading the spectral resolution, we have run the same 11 $M_\odot$ model, with the same spatial zoning and the same physics as in the baseline model, but with 20 and 10 energy groups. All three calculations were carried out to 250 milliseconds after bounce.

We observe only small quantitative differences and virtually no qualitative differences in the overall evolution of all quantities in comparing the run with 40 energy groups to that with only 20. Over the whole post-bounce evolution, $\langle \varepsilon_{\nu_e} \rangle$ is ~0.05 MeV higher in the 20-group calculation, a difference of just 0.5% at 250 ms. However, L_{ν_e} is higher by 2% in the model with just 20 energy groups. Differences in the average energy and luminosity of $\bar{\nu}_e$ and ν_μ neutrinos amount to less than ~1% overall, with each of these quantites lower in the 20-group calculation than in the model run with 40 energy groups. The basic hydrodynamical quantities were similarly unaffected. The core entropy was reproduced in the the 20-group model to within 0.5%, with the higher resolution model having slightly lower entropy. The core Y_e at bounce was just 0.5% lower in the model with 20 groups. The only qualitative difference observed between the two models was a slight oscillation in the velocity versus mass profile inside 0.5 $M_\odot$ just before bounce.

We find significant qualitative and quantitative differences between our 10-group model and our models with higher spectral resolution. The small oscillations observed in the matter velocity in the 20-group model are much more pronounced on infall with just 10 groups. There are similar and seemingly correlated oscillations in Y_e. Oscillations very similar to these have been observed in Rampp (2000) and Mezzacappa & Bruenn (1993c). The oscillations result from insufficient spectral resolution of the Fermi surface of electron neutrinos. In addition to the oscillations, many components of the hydrodynamic and neutrino spectral evolution are affected by the use of only 10 energy groups in our calculation. At bounce, the core entropy, which had come within 5% of that obtained in the 20- and 40-group calculations ($s_{\text{core}} \sim 1.35\ k_B$ baryon^{-1}), dropped to 0.8 k_B baryon^{-1}. This, of course, also manifests itself in the temperature profile. The core temperature after bounce reaches only 7.5 MeV, as compared with the 11 MeV obtained in the calculations with 20 and 40 energy groups. Despite the fact that the core Y_e was slightly higher in the 10-group calculation, the peak positive shock velocity just after bounce was 15% lower. The ν_e breakout pulse was 10% lower in the 10-group model than in the 40- or 20-group models. L_{ν_e} was ~ 0.03×10^{53} erg s^{-1} higher in the low-resolution model throughout the post-bounce evolution, this difference amounting to ~ 8% at 250 ms. In addition, we find that $L_{\bar{\nu}_e}(t)$ in the 10-group model peaks faster and higher than the 40-group model, but drops off more quickly in time. Although $L_{\bar{\nu}_e}$ at 250 ms is just 9% lower in the 10-group model than the 40-group model, the slope of the luminosity is steeper and that difference grows with time. The average energy for all species is higher in the 10-group calculation than in the 40-group calculation, but not by more than a few percent over the whole post-bounce evolution.

In sum, we conclude that 10 neutrino energy groups are insufficient for resolving the neutrino radiation field. We see the largest differences in the emergent spectrum for the electron neutrinos. This is likely due to the fact that the ε_{ν_e} grouping must extend to ~ 300 MeV in order to resolve the Fermi energy of the electron neutrinos within the core. Because ν_e transport, through the charged-current interaction, affects the dynamics so significantly, failure to resolve the ν_e radiation field affects most observables. Our model employing 20 energy groups comes quite close to reproducing our results with 40 energy groups. Differences are no larger than 2% and, for most quantities, the fractional differences are closer to 0.5−1%. Considering the large decrease in computation time (a factor of 2), 20 groups are probably desirable for all but the most detailed models. In comparison, with 21 energy groups Rampp (2000) finds that the ν_e Fermi surface is under-resolved, as the large oscillations he sees in the trapped lepton fraction demonstrate. Typical recent calculations by Rampp & Janka (2002) employ 20−30 energy groups spaced geometrically. Mezzacappa et al. (2001) and Liebendörfer et al. (2001) employ 12 energy groups.

5. COMPARISON BETWEEN PROGENITORS: 15 $M_\odot$ AND 20 $M_\odot$ MODELS

A complete theory of core-collapse supernovae must hope to understand the detailed dynamics and neutrino signatures of all possible supernova progenitors. If successful neutrino-driven supernova models were obtained, one might hope to find systematic trends between, for example, the progenitor mass and the peak neutrino luminosity, final supernova energy, or mass of the nascent protoneutron star. We begin such an investigation by first considering the dynamics and emergent neutrino characteristics of two more massive progenitors.

The top two panels of Fig. 13 show the L_{ν_e} (10^{54} erg s^{-1}, upper left-hand panel) and $L_{\bar{\nu}_e}$ and L_{ν_μ} (upper right-hand panel), at infinity as a function of time for three different progenitor masses: 11 $M_\odot$ (the baseline model, thick solid line), 15 $M_\odot$ (thin solid line), and 20 $M_\odot$ (dotted line). Note that the ν_e breakout pulse for each progenitor is remarkably similar, a result also recently obtained in the work of Liebendörfer et al. (2002a). Interestingly, as discussed in §3, our ν_e breakout pulse reaches ~ 2.55×10^{53} erg s^{-1}, whereas Liebendörfer et al. (2002a) obtain a characteristic peak L_{ν_e} of ~ 3.5×10^{53} erg s^{-1}. Note that our 20 $M_\odot$ model, which also employs 300 spatial zones, 40 neutrino energy groups, and the tangent-ray algorithm for angular binning, reaches a somewhat lower peak luminosity at ~ 2.225×10^{53} erg s^{-1}.

$L_{\bar{\nu}_e}$ and L_{ν_μ} are virtually identical in both the 11 $M_\odot$ and 15 $M_\odot$ models over the first 100 ms of post-bounce evolution and only later develop small differences. In marked contrast, the 20 $M_\odot$ model exhibits higher neutrino luminosities for all species after electron-neutrino breakout. For L_{ν_e} and $L_{\bar{\nu}_e}$, the difference between the 11 $M_\odot$ model and the 20 $M_\odot$ model is a factor of two at 200 milliseconds after bounce. For L_{ν_μ}, the difference is a factor of 1.5. In addition, L_{ν_μ} and $L_{\bar{\nu}_e}$ peak approximately 100 ms later in the 20 $M_\odot$ model than in the 11 $M_\odot$ progenitor.

Also shown in Fig. 13 (lower two panels) are the corresponding average neutrino energies (defined by eq. 2) of the emergent spectra. The lower left-hand panel shows the time evolution of $\langle \varepsilon_{\nu_e} \rangle$ and the lower right-hand panel shows the same for $\langle \varepsilon_{\bar{\nu}_e} \rangle$ and $\langle \varepsilon_{\nu_\mu} \rangle$. One hundred milliseconds after bounce the differences between the spectra from each model become significant. Not only are the spectra for the 20 $M_\odot$ model harder, but the average energies are increasing faster than those for the 11 $M_\odot$

and $15\,M_\odot$ models. Some of these systematics can be understood by inspecting Fig. 14, which shows the mass flux ($\dot{M}$) as a function of radius in units of $M_\odot$ s^{-1} for the $11\,M_\odot$ (thick solid line), $15\,M_\odot$ (thin solid line), and $20\,M_\odot$ (dotted line) models. Also shown are the positions of the neutrinosphere for the average emerging neutrino energy. Open triangles correspond to R_{ν_e}, whereas filled squares and open circles denote $R_{\bar{\nu}_e}$ and R_{ν_μ}, respectively. In the steady-state, the total luminosity of a given neutrino species should be given approximately by the accretion luminosity, written in terms of $\dot{M}$ and R_ν: $L_\nu^{\mathrm{acc}} \sim GM_\nu\dot{M}/R_\nu$, where M_ν is the mass enclosed by R_ν. This reflects the role of the neutrino luminosity in carrying away the energy of infall. To zeroth order, the higher mass flux in the $20\,M_\odot$ model in Fig. 14 explains the higher luminosity at that epoch in the top two panels of Fig. 13. This conclusion is modified slightly by the actual radial positions of the various neutrinospheres for each progenitor in this epoch and the mass enclosed within R_ν. Given the simple expression for L_ν^{acc}, the ratio of the total neutrino luminosity of the $20\,M_\odot$ model to that of the $11\,M_\odot$ model should be approximately

$$\frac{L_\nu^{20\,\mathrm{M}_\odot}}{L_\nu^{11\,\mathrm{M}_\odot}} = \left(\frac{M_\nu^{20\,\mathrm{M}_\odot}}{M_\nu^{11\,\mathrm{M}_\odot}}\right)\left(\frac{\dot{M}^{20\,\mathrm{M}_\odot}}{\dot{M}^{11\,\mathrm{M}_\odot}}\right)\left(\frac{R_\nu^{11\,\mathrm{M}_\odot}}{R_\nu^{20\,\mathrm{M}_\odot}}\right) \sim 2.5.$$

We find that the actual ratio, as obtained by solving the full problem, is ~ 1.9. These significantly higher neutrino luminosities in the post-bounce phase and slightly harder average energies affect the number of neutrino events we expect from the next galactic supernova. In §8 we present detection results for each progenitor.

Although we obtain higher average neutrino luminosities and energies for the $20\,M_\odot$ progenitor, there is no sign of explosion or developing explosion in this model. In fact, approximately $200\,\mathrm{ms}$ after bounce the shock in this progenitor has reached $r \sim 190\,\mathrm{km}$ and begins to recede; at approximately $250\,\mathrm{ms}$, it has dropped to $r \sim 150\,\mathrm{km}$. In contrast, both the $11\,M_\odot$ and $15\,M_\odot$ progenitors maintain shock radii of 180-190 km throughout this epoch. Although none of these simulations yields an explosion, the lower mass models seem more promising.

6. DEPENDENCE ON THE NUCLEAR EQUATION OF STATE

One might expect that large modifications to the nuclear equation of state could have a significant impact on the collapse and bounce dynamics, as well as on the emergent neutrino spectra. We have not yet studied nuclear equations of state based on finite-temperature mean-field theory, nor have we incorporated exotic particle species and phase transitions. Such equations of state are of considerable interest, but are not always easily incorporated into existing dynamical codes. In addition, the neutrino microphysics would have to be made consistent with the presence of exotic constituents (e.g., neutrino-meson and neutrino-quark interactions) (Reddy, Prakash, & Lattimer 1998).

Performing an albeit limited exploration of the parameter space available to high-density equations of state, we have constructed three tabular versions of the LSEOS (see Appendix §A) with different nuclear compressibilities: $\kappa = 180$, 220, and 375 MeV. For all of our baseline models we took $\kappa = 220$ MeV. Note that, since Lattimer and Swesty (1991) attempted to construct a thermodynamically-consistent EOS with self-consistent

Maxwell constructions at the phase transition to nuclear matter, LSEOS models with different compressibilities also have different $\hat{\mu}$s, compositions, and energies, not just pressures.

In order to illustrate the role of the "nuclear compressibility," we have run collapse and bounce simulations with all three κs, evolving each to $200\,\mathrm{ms}$ after bounce. Figure 16 shows the temperature profile in an $11\,\mathrm{M}_\odot$ progenitor for calculations with $\kappa = 180$ (dashed lines) and $\kappa = 375$ (solid lines) $\sim 2\,\mathrm{ms}$ and $\sim 100\,\mathrm{ms}$ after bounce. The model with $\kappa = 180$ reaches a higher core temperature, but has a steeper negative temperature gradient, reaching a minimum at M$\simeq 0.4$ $M_\odot$. The peak temperature at M$\simeq 0.65$ $M_\odot$ is also higher for the lower compressibility model. Overall, however, the two models are remarkably similar. Peak velocities in both calculations reach $\sim 2 \times 10^9$ cm s^{-1} at M~ 0.7 $M_\odot$. In addition, the entropy and Y_e profiles are qualitatively identical for all three κs. Although the ν_e breakout luminosity pulse for the model with $\kappa = 375$ is delayed by 1 ms compared with the corresponding pulse for both $\kappa = 180$ and $\kappa = 220$, the shape and magnitude of the pulses are very similar.

Figure 17 shows that for both EOS models the luminosities at the edge of the grid for all neutrino species (apart from the 1 ms offset for $\kappa = 375$) evolve similarly during the first $\sim 30\,\mathrm{ms}$ after bounce. The average neutrino energies for both EOS models are also similar during this earlier phase. After $50\,\mathrm{ms}$, the differences between the models with $\kappa = 180$ and $\kappa = 375$ in both the neutrino luminosities and spectra become discernible. The post-bounce neutrino luminosity for all species is lower in the $\kappa = 375$ model. At $200\,\mathrm{ms}$ after bounce the fractional difference is approximately 4%, 5%, and 9% for L_{ν_e}, $L_{\bar{\nu}_e}$, and L_{ν_μ}, respectively. The model with $\kappa = 375$ also produces characteristically softer spectra with the average energy for each species being $\sim 3\%$ lower. Although $\langle \varepsilon_{\nu_e}\rangle$ and $\langle \varepsilon_{\bar{\nu}_e}\rangle$ are lower by a few percent in the model with $\kappa = 375$, $\langle \varepsilon_{\nu_\mu}\rangle$ is not evolving to higher energies as quickly as in the model with $\kappa = 180$. For all models, $\langle \varepsilon_{\nu_\mu}\rangle$ evolves approximately linearly with time, but the model with $\kappa = 180$ (the softer EOS) evolves with a larger slope. In §8.4 we quantify the importance of the nuclear compressibility modulus in shaping the detected neutrino signal from supernovae.

These differences in spectra and some of the basic hydrodynamical quantities are not large enough to affect the post-bounce dynamics significantly on 100 ms timescales. In fact, $200\,\mathrm{ms}$ after bounce, there is very little difference between the shock position, gain radius, or neutrinosphere positions in these two models. Perhaps larger differences between models with different compressibilities develop on one- and ten-second timescales in the post-explosion protoneutron star cooling epoch. This might be important both for detectability of the neutrino signature at late times and the evolution of the neutrino-driven protoneutron star wind (Thompson, Burrows, and Meyer 2001).

7. MODIFICATIONS TO THE STANDARD CROSS SECTIONS AND SOURCES

The work of Burrows & Sawyer (1998,1999), Raffelt & Seckel (1998), Janka et al. (1996), and Reddy, Prakash, & Lattimer (1998) all point to a reduction at high density of the dominant neutral- and charged-current opacity sources for neutrinos due to nucleon-nucleon correlations caused by the strong

interaction and Fermi statistics. Such modifications to the standard neutrino opacities depend on the model for strong interactions employed. Ideally, they should be included consistently in constructing the nuclear equation of state (Reddy, Prakash, & Lattimer 1998). Although they did not take into account these changes to the nuclear EOS, Rampp et al. (2002) have recently investigated the role of nuclear correlations in their dynamical models. They found modest enhancements in L_{ν_e} and L_{ν_μ} and considerable enhancements in $L_{\bar{\nu}_e}$ ($\sim 20\%$). Although inclusion of these processes did not lead to explosions, they did affect the dynamics and it seems they should not be absent from a full treatment of the problem.

In a future work we will incorporate the dynamical structure function formalism of Burrows & Sawyer (1998,1999) and Reddy, Prakash, & Lattimer (1998). For now, we provide a set of simple tests, varying some of our cross sections and reaction rates in order to test the sensitivity of the observables and the dynamics.

7.1. *Artificial Opacity Reduction*

In Liebendörfer (2000), erroneous explosions were obtained in one-dimensional models of supernovae because of an artificially decreased neutral-current neutrino-nucleon opacity. As a simple test, we have decreased the neutrino-neutron (σ_n) and neutrino-proton (σ_p) scattering cross sections by a factor of 10 everywhere, for all neutrino energies. Despite such a change, because the dynamics during collapse and bounce are dominated by neutral-current scattering on nuclei and the charged-current process $\nu_e n \leftrightarrow e^- p$, the breakout phenomenon is only modestly affected; the peak ν_e breakout pulse is just 10% higher than in our baseline model and reaches 2.85×10^{53} erg s^{-1}. Two hundred and fifty milliseconds after breakout, $L_{\nu_e} \simeq 0.25 \times 10^{53}$ erg s^{-1} in our baseline model. In our model with $\sigma_{n,p}/10$, we obtain $L_{\nu_e} \simeq 0.35 \times 10^{53}$ erg s^{-1}. Figure 15 shows L_{ν_e} and $L_{\bar{\nu}_e}$ at infinity as a function of time for the baseline model and the model presented here. Both L_{ν_e} and $L_{\bar{\nu}_e}$ are increased by ~ 40–50% in the calculation with lower opacity. These changes, however, are modest compared with those for L_{ν_μ} and $\langle \varepsilon_{\nu_\mu} \rangle$. Two hundred and fifty milliseconds after bounce, L_{ν_μ} equals 2.4×10^{53} erg s^{-1}, a factor of four larger than in the baseline model. For ν_μ neutrinos, there is no charged-current absorption process on free nucleons to contribute to the total opacity, as there is for the ν_e and $\bar{\nu}_e$ neutrinos. For the ν_μs, the neutral-current scattering dominates the opacity and so changing that opacity source so dramatically has significant consequences for L_{ν_μ} and $\langle \varepsilon_{\nu_\mu} \rangle$.

Importantly, because of the increase in the L_{ν_e} and $L_{\bar{\nu}_e}$ we obtain a larger gain region in this calculation, higher entropy behind the shock, and a larger shock radius 250 ms after bounce. In the baseline model, at 250 ms post-bounce the shock is sitting at 180 km, whereas in the model with reduced opacities, $R_s \simeq 210$ km. Still, although the dynamics are affected by this drastic decrease in neutrino opacity, we do not obtain an explosion in this first 250 ms of post-bounce evolution.

7.2. *The Weak Magnetism/Recoil Correction*

Our baseline 11 $M_\odot$ model includes the weak magnetism/recoil correction to the charged-current opacities for ν_e and $\bar{\nu}_e$ and to the neutral-current scattering opacities off of nucleons for all neutrino species (Vogel 1984; Horowitz 1997,2002). The weak magnetism/recoil correction lowers the cross section for all processes; the decrease is largest for anti-neutrinos ($\bar{\nu}_e$ and $\bar{\nu}_\mu$). We ran our baseline model (§3) without these corrections and found only small differences in the first 250 milliseconds of post-bounce evolution. L_{ν_e}, L_{ν_μ}, $\langle \varepsilon_{\nu_e} \rangle$, and $\langle \varepsilon_{\nu_\mu} \rangle$ are all lower at the 0.5% level without the weak-magnetism correction. $\langle \varepsilon_{\bar{\nu}_e} \rangle$ and $L_{\bar{\nu}_e}$ are less by 4% in this representative 11 $M_\odot$ calculation. This slight softening and dimming of the emergent spectra can be understood simply as the result of increasing the total opacity for all species by removing the small weak magnetism/recoil correction. Hence, though the corrections themselves for given temperatures, densities, and neutrino energies can be greater than 10–15%, due to feedbacks on the dynamics and thermodynamics, the self-consistent inclusion of weak-magnetism/recoil effects in a core-collapse calculation has only very limited consequences.

7.3. *The Role of Nucleon-Nucleon Bremsstrahlung*

The effects of bremsstrahlung on the ν_e and $\bar{\nu}_e$ spectra are negligible at virtually all times because for them the charged-current processes $\nu_e n \leftrightarrow pe^-$ and $\bar{\nu}_e p \leftrightarrow ne^+$ dominate. Thompson, Burrows, and Horvath (2000) and Raffelt (2001) showed that nucleon-nucleon bremsstrahlung might have important consequences for the emergent ν_μ spectra and that it dominates $e^+ e^- \rightarrow \nu_\mu \bar{\nu}_\mu$ as a production process. Figure 18 shows the effect of bremsstrahlung on the average energy of ν_μs. The plot itself shows the average energy (in MeV) as a function of radius approximately 230 ms after bounce. The inset shows $R_{\nu_\mu}(\varepsilon_{\nu_\mu})$, the neutrinosphere radius, defined by eq. (1), as a function of energy. The solid line is the baseline model, with neutrino-electron scattering redistribution and nucleon-nucleon bremsstrahlung. The short dashed line is the same model run through the full evolution, but without nucleon-nucleon bremsstrahlung. The long dashed line shows the same model without neutrino-electron scattering energy redistribution, but with nucleon-nucleon bremsstrahlung. One can see immediately from the inset that at low energies, bremsstrahlung increases the opacity significantly. It is also clear from the main figure that inelastic neutrino-electron scattering profoundly effects the emergent ν_μ spectrum.

Figure 19 shows L_{ν_μ} and $\langle \varepsilon_{\nu_\mu} \rangle$ at infinity as a function of time for the baseline model (thick solid line), which includes nucleon-nucleon bremsstrahlung, and the same model computed without bremsstrahlung (thin solid line). With bremsstrahlung, the average energies of the ν_μ neutrinos are lower and the luminosity is significantly higher. The results of Thompson, Burrows, and Horvath (2000) anticipated these results based on comparisons between the bremsstrahlung and $e^+ e^-$-annihilation neutrino production rates. Near the ν_μ neutrinosphere, the bremsstrahlung emission spectrum is peaked at low neutrino energies (< 10 MeV) compared with $e^+ e^-$ annihilation. For this reason, Thompson, Burrows, and Horvath (2000), Burrows et al. (2000), and Raffelt (2001) concluded that the emergent ν_μ spectra have both higher luminosity and lower average energy. As evidenced by Fig. 19, this prediction is borne out in our dynamical models.

7.4. *The Effects of Inelastic Neutrino-Electron Scattering*

Figure 20 shows the luminosity at infinity as a function of time for all species in the $11\,\mathrm{M}_\odot$ models with (thin solid line) and without (thick solid line) inelastic neutrino-electron scattering, using the prescription described in detail in Appendix B.1. Figure 21 shows the *rms* neutrino energy for each species for the model without inelastic $\nu_i e^-$ scattering and should be compared with Fig. 7. The main ν_e breakout pulse is enhanced slightly and reaches 2.73×10^{53} erg s^{-1}, compared with 2.55×10^{53} erg s^{-1} in the baseline model. Also noticeable in L_{ν_e} is the decrease in the pre-breakout pulse associated with the deleptonization of the core on infall as described in §3. Shown here at $t \sim 0.007\,\mathrm{s}$, the pre-breakout peak reaches 0.75×10^{53} erg s^{-1} with neutrino-electron scattering and only 0.52×10^{53} erg s^{-1} without. By downscattering neutrinos during collapse and bounce via $\nu_e e^-$ scattering, more neutrinos are able to escape before the core becomes opaque. Thus, there is a trade-off. Including inelastic scattering off electrons makes the *collapse* luminosity peak higher, but the main *breakout* luminosity peak lower. Although the breakout phenomenon is slightly affected, the spectra of ν_e and $\bar{\nu}_e$ neutrinos at 200 ms are dominated by the charged-current interactions and so the effects of νe^- scattering on L_{ν_e}, $L_{\bar{\nu}_e}$, $\langle\varepsilon_{\nu_e}\rangle$, and $\langle\varepsilon_{\bar{\nu}_e}\rangle$ are modest. ν_μ neutrinos are more significantly affected. Throughout the evolution, L_{ν_μ} is decreased by $\sim 30\%$ by including $\nu_\mu e^-$ redistribution. $\langle\varepsilon_{\nu_\mu}\rangle$ is also profoundly altered. Comparing Fig. 21 with Fig. 7, we see that $\langle\varepsilon_{\nu_\mu}\rangle$ is ~ 6 MeV higher without $\nu_\mu e^-$ redistribution.

Figure 2 shows that there is significantly more deleptonization of the core at bounce with inelastic neutrino-electron scattering (thick solid line) than there is without it (long dashed line). The magnitude of the difference in core Y_e at bounce is in keeping with other recent models (cf. Rampp 2000, §3). The fact that Y_e^{core} is higher at bounce in the latter case has important consequences for the shock energy and the early postbounce neutrino characteristics. In the model without neutrino-electron scattering, the peak positive velocity after bounce is higher ($\sim 2.5\times10^9$ cm s^{-1}, compared with $\sim 2.0\times10^9$ cm s^{-1}) and peaks at larger interior mass ($0.85\,\mathrm{M}_\odot$, compared with $0.7\,\mathrm{M}_\odot$). In both models, as the shock stalls and the briefly positive velocities achieved become negative, the matter behind the shock (the protoneutron star) oscillates on $5-10$ millisecond timescales. As the protoneutron star pulsates, pressure waves move through the neutrinosphere of each species. These waves act to modulate the emergent luminosity and average neutrino energy. The amplitude of these near-periodic variations in neutrino luminosity and energy are damped on ~ 10 ms timescales. They are smaller for the model with neutrino-electron scattering because the shock in this model has less energy and the corresponding post-bounce oscillatory mass motions ('ringing') are thereby smaller at the neutrinosphere for each species. The smaller the local changes in temperature and density near the neutrinosphere, the smaller the changes in the local emission and absorption. Hence, we should expect smaller amplitude temporal modulations in the emergent neutrino spectral characteristics.

Also potentially important is the fact that $L_{\bar{\nu}_e}$ rises later in the model with neutrino-electron energy redistribution than in the model without such redistribution. Twenty milliseconds after bounce, Fig. 20 shows that $L_{\bar{\nu}_e}$ with $\nu_i e^-$ scattering is approximately half that for the model without this thermalization process. This has important implications for the detection of the ν_e breakout pulse in terrestrial light-water Čerenkov neu-

trino detectors like SuperKamiokande. In §8.1, we show that in such detectors, if one is to identify the ν_e breakout signature uniquely, one must do so within $5-20$ milliseconds of bounce, but before the $\bar{\nu}_e$ signal becomes appreciable. Hence, because neutrino-electron scattering suppresses the $\bar{\nu}_e$ signal during this epoch, it has consequences for the observation of the next galactic supernova.

8. NEUTRINO DETECTOR SIGNATURES

A total of just 19 neutrino events were observed from supernova SN1987A in the IMB (Irvine-Michigan-Brookhaven) and Kamioka II detectors. The signal lasted ~ 10 seconds and confirmed the basics of our theoretical understanding of core collapse; the amount of energy radiated in neutrinos was comparable to that expected in protoneutron star cooling models at the time (Burrows & Lattimer 1986) and the inferred $\bar{\nu}_e$ neutrino spectra had average energies of ~ 10–15 MeV (compare with Fig. 7).

Far surpassing the sensitivity of Kamioka II and IMB, the current generation of neutrino detectors might collectively see thousands of neutrino events from the next galactic supernova (Burrows, Klein, & Gandhi 1992). Such an event would provide exquisite neutrino spectral information and would put strong constraints on the physics of the core during collapse and explosion. Besides elucidating supernova physics, much information on the mass hierarchy of neutrinos could also be collected. For example, the neutrino signature might clearly reveal whether a black hole or a neutron star had been created (Burrows 1988) and if the former is born, direct eV-scale measurements of ν_μ- and ν_τ-neutrino masses could be made by the current generation of detectors (Beacom, Boyd, & Vogel 2000).

Using the models presented in the preceding sections, we have made predictions about the dynamics and emergent neutrino spectra expected from a class of supernova progenitors, with reasonable variations in microphysics and the models. In this section, we go a step further and fold our neutrino spectra with the thresholds and sensitivities of a subset of modern neutrino detectors. The focus is on the detectability of the breakout phenomenon itself.

In underground light-water detectors, such as a fully-repaired Super Kamiokande (SK), we can expect ~ 5000 neutrino events from the next galactic supernova at a distance of 10 kpc. In such detectors the primary mechanism for neutrino detection is the $\bar{\nu}_e p \rightarrow n e^+$ process. The positron secondary emits Čerenkov radiation. For an electron or positron secondary, the differential number detected at distance D can be written (Burrows, Klein, & Gandhi 1992):

$$dN = \frac{N_T}{4\pi D^2} L_\nu^{\mathrm{num}}(t', \varepsilon_\nu) \frac{d\sigma(\varepsilon_\nu, \varepsilon_e)}{d\varepsilon_e}$$
$$\times E(\varepsilon_e)\delta(t - t' - \Delta t)\, dt'\, d\varepsilon_e\, d\varepsilon_\nu\, dt, \qquad (3)$$

where ε_e is the electron or positron energy, $E(\varepsilon_e)$ is the detection efficiency, N_T is the number of targets, L_ν^{num} is the number luminosity of neutrinos, t' is the source time, t is the detector time with D/c subtracted, $\Delta t(\simeq D/2c\,(m_\nu c^2/\varepsilon_\nu)^2)$ is the time delay of a neutrino with mass m_ν, and $d\sigma/d\varepsilon_e$ is the differential cross section for neutrino capture and electron or positron production. For most purposes $d\sigma/d\varepsilon_e \simeq \sigma(\varepsilon_\nu)\delta(\varepsilon_\nu - \varepsilon_e - \Delta)$, where Δ is the reaction threshold (in the case of the reaction $\bar{\nu}_e p \rightarrow n e^+$, $\Delta = m_n - m_p + m_e \simeq 1.804$ MeV). Taking this ap-

proximation for $d\sigma/d\varepsilon_e$, $E(\varepsilon_e) = 1$, and $m_\nu = 0$, we obtain

$$\frac{dN}{dt\,d\varepsilon_\nu} = \frac{N_T}{4\pi D^2} L_\nu^{\mathrm{num}}(t,\varepsilon_\nu)\sigma(\varepsilon_\nu). \tag{4}$$

Using eqs. (3) and (4), it is a relatively simple matter to fold our time-dependent spectra with terrestrial detector characteristics, including efficiency and threshold corrections, in order to obtain the observed neutrino signal. We consider three different detectors, focusing on the ν_e-rich breakout phase and the early neutrino signal that might be observed from the next galactic supernova. Although eq. (3) includes the effects of time-delay due to a finite neutrino mass, in what follows we assume massless neutrinos and employ eq. (4).

8.1. *SuperKamiokande*

The SuperKamiokande (SK) neutrino observatory is a light-water Čerenkov detector whose baseline volume for supernova neutrino detection is ~ 32 ktonne (Totani et al. 1998). We take as a threshold ~ 5 MeV (Beacom & Vogel 1998). The background is typically of order several $\times 0.1\,\mathrm{s}^{-1}$ if the full detector volume is considered (Beacom & Vogel 1998) and will not figure into our discussion here.

Light-water Čerenkov detectors offer several different channels for detection of the various neutrino species. The dominant reaction is charged-current absorption of $\bar{\nu}_e$ neutrinos on free protons ($\bar{\nu}_e p \to n e^+$). The positron secondary emits Čerenkov radiation, which is detected directly. Neutrino scattering on electrons, $\nu_i e^- \to \nu_i e^-$ also contributes for all neutrino species. For this process, we use the neutrino-electron scattering cross section (Sehgal 1974):

$$\frac{d\sigma_i}{d\varepsilon_e} = \frac{1}{2}\frac{\sigma_o}{m_e c^2}\left[A_i + \left(1 - \frac{\varepsilon_e}{\varepsilon_\nu}\right)^2 B_i\right]$$
$$\implies \sigma_i = \frac{1}{2}\sigma_o \Lambda_i\left(\frac{\varepsilon_\nu}{m_e c^2} + \frac{1}{2}\right), \tag{5}$$

where

$$\Lambda_i = \frac{1}{4}\left(A_i + \frac{1}{3}B_i\right), \qquad A_i = (C_V + C_A)^2, \qquad B_i = (C_V - C_A)^2,$$

and $C_V = \pm 1/2 + 2\sin^2\theta_W$ for electron types and muon types, respectively. $C_A = +1/2$ for ν_e and $\bar{\nu}_\mu$, and $C_A = -1/2$ for $\bar{\nu}_e$ and ν_μ. Note that the neutrino-electron scattering cross section is $6-7$ times less for the μ- and τ-type neutrinos, owing to the fact that for them the reaction can proceed via only the neutral current. Other important reactions include

$$\nu_e + {}^{16}\mathrm{O} \to {}^{16}\mathrm{F} + e^- \quad (\epsilon_{\mathrm{th}} = 15.4\,\mathrm{MeV}), \tag{6}$$

$$\nu_e + {}^{18}\mathrm{O} \to {}^{18}\mathrm{F} + e^- \quad (\epsilon_{\mathrm{th}} = 1.66\,\mathrm{MeV}), \tag{7}$$

$$\bar{\nu}_e + {}^{16}\mathrm{O} \to {}^{16}\mathrm{N} + e^+ \quad (\epsilon_{\mathrm{th}} = 11.4\,\mathrm{MeV}), \tag{8}$$

and

$$\nu_i + {}^{16}\mathrm{O} \to \nu_i' + {}^{16}\mathrm{O}^* \to \nu_i' + \gamma + X, \tag{9}$$

where ϵ_{th} is the energy threshold for the reaction. For the neutral-current excitation of ${}^{16}\mathrm{O}$ (reaction 9), the γ secondary has an energy in the range $5-10$ MeV and, hence, is detectable by SK. Note that energy resolution for the secondary electron or positron in reactions (6), (7), and (8) is good to no better than $\sim 10-20\%$ (Burrows, Klein, & Gandhi 1992; Totani et al. 1998). For the study carried out here, we calculate event

rates in SK due to only $\bar{\nu}_e p \to n e^+$ and neutrino-electron scattering for all neutrino species. We assume 100% efficiency above the detector threshold.

Figure 22 shows the integrated number of ν_e and $\bar{\nu}_e$ neutrino events ($\log_{10}[N(<t)]$) detected in SK for our baseline $11\,\mathrm{M}_\odot$ progenitor (thick lines) and for the $20\,\mathrm{M}_\odot$ progenitor (thin lines) described in §5. The ν_e neutrino signal from ν_e-electron scattering (labeled '$\nu_e e^- \to \nu_e e^-$') is the solid line for both progenitors. The $\bar{\nu}_e$ neutrino signal from charged-current absorption on free protons (labeled '$\bar{\nu}_e p \to n e^+$') is the dashed line for both progenitors. Note that many hundreds more $\bar{\nu}_e$ events accumulate from the $20\,\mathrm{M}_\odot$ progenitor (~ 1250) than from the $11\,\mathrm{M}_\odot$ (~ 650) progenitor in the $250\,\mathrm{ms}$ of post-bounce evolution shown here. This important difference results from the steeper density gradient outside the iron core in the $11\,\mathrm{M}_\odot$ progenitor and the correspondingly lower accretion luminosity (see Fig. 14). The inset in Fig. 22 shows the first 55 ms of the signal and the initial rise of the number ν_e neutrinos detected due to breakout. The inset shows that approximately 5 ν_e events can be expected from the collapse phase of the supernova, while $10-15$ ν_e events might be observed solely from the breakout neutronization burst. This result seems to be independent of the mass of the progenitor. Although we do not include the results for the $15\,\mathrm{M}_\odot$ progenitor (see §5) in Fig. 22, as indicated by Fig. 13, its ν_e breakout signature is virtually identical to that for the $11\,\mathrm{M}_\odot$ model. However, for the $15\,\mathrm{M}_\odot$ progenitor the luminosity of $\bar{\nu}_e$ neutrinos is slightly higher after 100 ms. As a result, 250 ms after bounce the integrated number of $\bar{\nu}_e$ events is $\sim 5\%$ higher than for the $11\,\mathrm{M}_\odot$ model.

Note that the combined neutral-current $\nu_{\mu,\tau}$ and $\bar{\nu}_{\mu,\tau}$ signal due to scattering off of electrons is much smaller than that due to the process $\nu_e e^- \to \nu_e e^-$. This signal never contributes significantly to the total neutrino event rate. In particular, less than 1 event due to μ- and τ-neutrino scattering on electrons should be observed in the first 50 ms.

Importantly for models of the neutrino oscillation phenomenon, the neutrino signal through collapse (~ 5 ν_e events), breakout ($10-15$ ν_e events), and just post-breakout (~ 5 ν_e events) should be composed of only ν_e neutrinos. The break in the total number of events observed, which must occur as the $\bar{\nu}_e$ neutrinos begin to dominate the signal just 20-30 ms after bounce, signals the end of this pure ν_e neutrino phase. In addition, because the reaction $\nu_e e^- \to \nu_e e^-$ is very forward-peaked and the process $\bar{\nu}_e p \to n e^+$ is slightly backward-peaked for $\varepsilon_{\bar{\nu}_e} \lesssim 15\,\mathrm{MeV}$ (Vogel & Beacom 1999), one might hope to distinguish the early $\bar{\nu}_e$ signal from the post-breakout ν_e neutrino signal based on the directionality of the Čerenkov cones left by the positron and electron secondaries. However, if there is large mixing between ν_e and ν_μ or ν_τ neutrinos, the early ν_e signal might be lessened significantly in SK (e.g. Takahashi et al. 2001).

8.2. *The Sudbury Neutrino Observatory*

The Sudbury Neutrino Observatory (SNO) in Sudbury, Ontario, is a light- and heavy-water neutrino detector. It is a spherical acrylic vessel 12 meters in diameter, containing 1 ktonne of D_2O, that is surrounded by a cavity filled with light water. The fiducial light-water mass is approximately 1.6 ktonne. SNO is most sensitive to ν_μ and $\bar{\nu}_\mu$ neutrinos via breakup reactions on deuterons:

$$\nu_i + d \to n + p + \nu_i \quad (\epsilon_{\mathrm{th}} = 2.22\,\mathrm{MeV}) \tag{10}$$

$$\bar{\nu}_i + d \rightarrow n + p + \bar{\nu}_i \quad (\epsilon_{\text{th}} = 2.22\,\text{MeV}). \tag{11}$$

The liberated neutron secondary is thermalized in the heavy water and is then detected via capture on other nuclei within the detector volume. Currently, the neutrons from neutral-current events are detected via deuteron capture with an efficiency of $\sim 30\%$ (Ahmad et al. 2002; SNO Collaboration). Several schemes are currently proposed and in development for improved neutron-capture efficiency. The first is to lace the D_2O with two tonnes of NaCl. The thermal neutron absorption cross section on ^{35}Cl is large ($\sim 83\%$ efficiency) and would result in a γ cascade peaked at 8 MeV. The γs would be detected by the ~ 9600 inward-looking photomultiplier tubes outside of the acrylic vessel. The second proposed neutron detection method involves hanging ^3He proportional counters in the acrylic vessel and these would detect the neutrons directly (SNO collaboration webpage[3]). Because the neutrons would have a ~ 5 ms mean capture time if the ^{35}Cl capture mechanism is employed (which would spread the ν_μ turn-on), the neutral-current signal might be partially smeared with the ^{35}Cl approach. The neutral-current deuteron breakup reactions (reactions 10 and 11) also contribute to the ν_e and $\bar{\nu}_e$ signal in SNO, but for them the charged-current deuteron capture processes,

$$\nu_e + d \rightarrow p + p + e^- \quad (\epsilon_{\text{th}} = 1.44\,\text{MeV}) \tag{12}$$

$$\bar{\nu}_e + d \rightarrow n + n + e^+ \quad (\epsilon_{\text{th}} = 4.03\,\text{MeV}), \tag{13}$$

are more important above $\varepsilon_\nu \simeq 10$ MeV (Burrows, Klein, & Gandhi 1992). Process (13) can be used to observe $\bar{\nu}_e$ neutrinos uniquely via the simultaneous detection of the secondary neutron and the Čerenkov emission from the final-state positron. Although we include the threshold energy in our calculations of the total signal, as with SK we assume a 100% efficiency for SNO above the detector theshold.

In Fig. 23 we show the integrated number of ν_e neutrinos detected in SNO via the processes $\nu_e d \rightarrow ppe^-$ (dotted line), $\nu_e d \rightarrow np\nu_e$ (solid line), and $\nu_e e^- \rightarrow \nu_e e^-$ (dashed line) in the first 250 ms after bounce in our $11\,M_\odot$ baseline model. The total ν_e signal is the thick solid line. For comparison, we provide the contribution to the total number of detected events from all other neutrino species (long dashed line, labeled 'Total(other)'). This signal includes the $\bar{\nu}_e d \rightarrow np\bar{\nu}_e$, $\bar{\nu}_e d \rightarrow nne^+$, and $\bar{\nu}_e p \rightarrow ne^+$ processes in the light-water portion of the detector, as well as the processes $\bar{\nu}_{\mu,\tau} d \rightarrow np\bar{\nu}_{\mu,\tau}$, $\nu_{\mu,\tau} d \rightarrow np\nu_{\mu,\tau}$, and neutrino-electron scattering throughout the entire detector volume. Note that it might be possible to exclude the charged-current absorption process $\bar{\nu}_e d \rightarrow nne^+$ by cutting on events that have simultaneous neutron and positron detection. This would lower somewhat the line labeled *Total(other)* and make the early ν_e breakout signal easier to see. However, such a procedure requires accurate signal timing, which would be a challenge if the ^{35}Cl neutron capture mechanism is employed. As it stands, one might expect to get ~ 5 events in SNO from the ν_e breakout burst in the first ~ 10 ms after bounce.

8.3. *ICARUS*

Although it has not yet reached its goal mass, ICARUS[4] is designed to be a 3.6-ktonne drift chamber of pure liquid ^{40}Ar that will be sensitive primarily to electron neutrinos through electron-neutrino capture on Ar:

$$\nu_e + ^{40}\text{Ar} \rightarrow ^{40}\text{K}^* + e^-.$$

Recent shell-model calculations have shown that this process can proceed through super-allowed Fermi transitions to the 4.38 MeV excited isobaric analog state, as well as through several Gamow-Teller (GT) transitions to other lower-lying states in ^{40}K (Ormand et al. 1995). This has recently been investigated experimentally by studying the β^+–decay from ^{40}Ti (Bhattacharya et al. 1998). Employing isospin symmetry, Bhattacharya et al. (1998) inferred the transition strengths of $^{40}\text{Ar} \rightarrow ^{40}\text{K}$ from $^{40}\text{Ti} \rightarrow ^{40}\text{Sc}$. These theoretical and experimental results indicate that the GT transitions enhance the total ν_e capture cross section by a factor of three over the pure Fermi transition cross section. We take the super-allowed Fermi transition cross section from Raghavan (1986);

$$\sigma_{\text{F}} \simeq 1.02 \times 10^{-43}(\varepsilon_{\nu_e} - 5.365)^2\,\text{cm}^2 \quad (\epsilon_{\text{th}} = 5.885\,\text{MeV}) \tag{14}$$

and we assume that the total ν_e absorption cross section is given by $\sigma_{\nu_e \text{Ar}}^{\text{tot}} = 3\sigma_{\text{F}}$.

The ICARUS detector is currently at 600 tonnes and has recently been approved to expand to 3 ktonnes. Because of its sensitivity to ν_e neutrinos, ICARUS is of particular importance in detecting the early breakout pulse so prominent in Fig. 6. In the results presented below, we assume that the detector efficiency is 100% above threshold and that the detector mass is 3 ktonnes.

The ν_e breakout signal in ICARUS is very likely detectable. Figure 24 shows $N(< t)$ for the ICARUS detector (with 3 ktonnes of Ar). We plot the two dominant detection channels for ν_e neutrinos: ν_eAr absorption (thick solid line) and $\nu_i e^- \rightarrow \nu_i e^-$ (thin solid line). We also include the event rate, dN/dt (in units of $50\,\text{s}^{-1}$), so that the width of the ν_e breakout spike can be compared with the detector signal in the very early phase. Note that the other neutrino species will contribute to the total signal through only the $\nu_i e^- \rightarrow \nu_i e^-$ process and that the combined signal amounts to only two events in the first 250 ms shown in Fig. 24. Combining the ν_e-electron scattering and ν_e-Ar absorption rates, ICARUS should expect to detect approximately 10 ν_e events from the breakout pulse alone, more than SNO and as many as Super K.

8.4. *The Influence on the Signal of Various Neutrino Processes and the EOS*

8.4.1. *Weak Magnetism & Recoil*

The weak-magnetism/recoil correction is relevant both in the supernova itself and in the detection of $\bar{\nu}_e$ neutrinos in light-water detectors via the process $\bar{\nu}_e p \rightarrow ne^+$. In §7.2 we compared the resulting spectra from models of core-collapse with and without this correction. In all our detection calculations we retain the weak-magnetism/recoil correction in calculating the signal due to $\bar{\nu}_e p \rightarrow ne^+$. Comparing the detector signal with and without this correction we find differences in events rates for neutrinos of all flavors of less than 1%. The models that include the correction have slightly higher event rates. For anti-neutrinos, in particular for $\bar{\nu}_e$ in SK, we find that the event rate with the correction is larger by approximately 7%.

8.4.2. *Inelastic Neutrino-Electron Scattering*

Inelastic neutrino-electron scattering in our core-collapse models significantly affects the observed ν_μ neutrino signal. The total ν_μ event rate in SK via neutrino-electron scattering 200 ms after bounce is $\sim$15% higher in the model without inelastic neutrino-electron scattering in the supernova. If this process is neglected in the supernova models, the signal in SNO due to neutral-current deuteron breakup by ν_μ neutrinos is nearly doubled. Approximately 200 ms after bounce, the corresponding event rates are $110\,\mathrm{s}^{-1}$ and $65\,\mathrm{s}^{-1}$, respectively.

Inelastic neutrino-electron scattering also affects the observed early-time $\bar{\nu}_e$ signal in SK. Figure 20 demonstrates that the $\bar{\nu}_e$ luminosity very near breakout is larger in the model without neutrino-electron scattering, though at later times models with and without neutrino-electron scattering are quite similar. At 200 ms after bounce, we obtain in SK 50 more $\bar{\nu}_e$ events in the model without neutrino-electron scattering (550 versus 500 events). Just 20-30 ms after bounce, the event rates differ by 10-15%.

8.4.3. *Nucleon-Nucleon Bremsstrahlung*

Including nucleon-nucleon bremsstrahlung as a production process for ν_μ neutrinos softens and brightens the resulting spectrum (see §7.3 and Fig. 18). By including bremsstrahlung, the total event rate in SNO due to neutral-current deuteron breakup by ν_μ neutrinos 200 ms after bounce is increased by 13%. Similarly, the total number of neutrino-electron scattering ν_μ events in SK is increased by 20% (10.5 versus 8.5 events after 200 ms). The event rates during this epoch of accretion-driven neutrino luminosity are $62\,\mathrm{s}^{-1}$ and $55\,\mathrm{s}^{-1}$, respectively - a fractional difference of $\sim$11%.

8.4.4. *LSEOS*

In §6, we presented results from core-collapse calculations employing different nuclear compressibilities in the context of the LSEOS (see Appendix A). In the model with $\kappa = 180\,\mathrm{MeV}$ we find that the ν_e-electron scattering event rate in SK 200 ms after bounce is $160\,\mathrm{s}^{-1}$ and that the corresponding cumulative event total is 47. The model with $\kappa = 375\,\mathrm{MeV}$ gives $150\,\mathrm{s}^{-1}$ and 42, respectively. The event rates in SK due to $\bar{\nu}_e$ capture on free protons 200 ms after bounce are $2870\,\mathrm{s}^{-1}$ and $3080\,\mathrm{s}^{-1}$ for $\kappa = 375\,\mathrm{MeV}$ and $\kappa = 180\,\mathrm{MeV}$, respectively - a fractional difference of just $\sim$7%. The ν_μ signal in both SK (due to neutrino-electron scattering) and in SNO (due to deuteron breakup) are modified at the 10% level, with the larger event rates corresponding to the lower nuclear compressibility ($\kappa = 180\,\mathrm{MeV}$).

8.5. *Neutrino Oscillations*

Due to severe matter suppression of standard flavor neutrino oscillations at the high densities encountered in supernova cores, such oscillations do not appreciably affect the dynamics, neutrino spectra, nor neutrino luminosities in the interior. We have calculated a few models that approximately incorporate flavor oscillations employing the oscillation parameters implied by the solar neutrino and atmospheric neutrino deficits and find almost no effect on core evolution.

The standard Boltzmann equation involves intensities, not amplitudes and phases. It is the evolution equations for the latter, or for a full density matrix, that should be calculated in order to take neutrino oscillations properly into account. However, we have opted for a simpler approach that captures the basic effect. For a freely propagating electron neutrino, the probability that it oscillates into a ν_μ neutrino is:

$$P_{e\mu} = \sin^2 2\theta_m \sin^2\left(\frac{\pi r}{L_m}\right), \qquad (15)$$

where θ_m and L_m are the oscillation angle and length in matter, r is the distance propagated, and θ is the oscillation angle in vacuum. L_m and θ_m are given by the expressions:

$$\sin^2 2\theta_m = \frac{\sin^2 2\theta}{\sin^2 2\theta + (\cos 2\theta - L_v/L_0)^2}, \qquad (16)$$

and

$$L_m = L_v\left[1 - \frac{2L_v}{L_0}\cos 2\theta + \left(\frac{L_v}{L_0}\right)^2\right]^{-1/2} = L_v\frac{\sin 2\theta_m}{\sin 2\theta}, \qquad (17)$$

where

$$L_v = \frac{4\pi\hbar\varepsilon_\nu}{\delta m^2 c} \sim 500\,\mathrm{km}\left(\frac{\varepsilon_\nu}{10\,\mathrm{MeV}}\right)\left(\frac{5\times 10^{-5}\,\mathrm{eV}^2}{\delta m^2}\right) \qquad (18)$$

is the vacuum oscillation length, $L_0 \sim 3.3 \times 10^{-3}\,\mathrm{cm}/\rho_{12}$, $\rho_{12} = \rho/10^{12}\,\mathrm{g\,cm^{-3}}$, and δm^2 is the standard mass-squared-difference. The matter suppression of neutrino flavor oscillations is quite severe. At resonance, $\theta_m = \pi/4$ and $L_v/L_0 = \cos 2\theta$, but for the range of densities that obtain in protoneutron stars and the values of δm^2 ($\sim 5 \times 10^{-5}\,\mathrm{eV}^2$) and $\sin^2 2\theta$ (> 0.8) derived from the KamLAND (Eguchi et al. 2003) and solar neutrino data, there are no MSW resonances in supernova interiors. We have not taken into consideration the possibility of density fluctuations induced neutrino flavor depolarization (Loreti et al. 1995). If we assume that a hard scattering or absorption decoheres the state ("resets the clock"), then a rough measure of the probability of oscillation from ν_e to ν_μ in a radius interval dr is $P_{e\mu}e^{-r/\Lambda}dr/\Lambda$, where Λ is the extinction mean-free path. The appropriate integral gives us the approximate transition rate

$$\Gamma_{e\mu} = \frac{2\pi^2 c}{\Lambda_e}\sin^2\theta_m\left(\frac{\Lambda_e}{L_m}\right)^2. \qquad (19)$$

There are corresponding expressions for $\Gamma_{\mu e}$, etc. These rates are plugged into rate equations that conserve total neutrino number:

$$\frac{dJ_{\nu_e}}{dt} = -\Gamma_{e\mu}J_{\nu_e} + \Gamma_{\mu e}J_{\nu_\mu}/4$$
$$\frac{dJ_{\nu_\mu}}{dt} = \Gamma_{e\mu}J_{\nu_e} - \Gamma_{\mu e}J_{\nu_\mu}/4, \qquad (20)$$

where J_i is the energy dependent zeroth moment of the specific intensity for neutrino species i ($\times 4$ for the ν_μs). Hence, using eqs. (20), we can incorporate the effects of neutrino oscillations on the internal supernova dynamics and spectra. As stated, they are small.

The edge of our computational grid resides deep inside the supernova progenitor. The spectra we have calculated and folded with terrestrial neutrino detectors will undoubtedly be modified by oscillation effects in propagating from the edge of our computational domain to the detector through the low-density progenitor envelope. Hence, our neutrino number spectra must be multiplied by effective survival probabilities taking into account the density profile of the overlying progenitor and, depending upon the position of the detector, the strata of

the Earth itself. Because our focus is here on producing reliable emergent spectra from core-collapse and the diagnosis of the basic effects on this signal of changes in the supernova microphysics, and because modifications to the signal in detectors depends on the wide range of progenitor envelope profiles, oscillation parameters, and Earth day-night effects, we save a detailed investigation of neutrino oscillations for a future work. The reader is referred to Ando & Sato (2002), Dighe & Smirnov (2000), Dutta et al. (1999), and Takahashi et al. (2001) for recent discussions of possible neutrino oscillation effects in the detected supernova neutrino signal.

9. SUMMARY AND DISCUSSION

We have constructed fully dynamical models of core collapse in spherical symmetry, focusing on the shock breakout phenomenon and the first 100's of milliseconds after bounce. We employed a newly-developed algorithm for radiation-hydrodynamics, which gives a Boltzmann solution to the neutrino transport problem using the Feautrier technique, the tangent-ray method, and Accelerated Lambda Iteration. The code provides good angular and spectral resolution of the radiation field and incorporates realistic neutrino microphysics. We find that at least 20 energy groups are required to adequately resolve the neutrino spectrum and the dynamics; 10 energy groups are not enough. Furthermore, the tangent-ray algorithm provides very good and adaptive angular resolution that is well-suited to the spherically-symmetric supernova problem in which the neutrino fields transition from a diffusive interior to a free-streaming exterior that nevertheless still resides within the relevant computational domain. Using this scheme, we have presented some of the first high-resolution angular distribution functions for neutrinos in stellar collapse.

We have explored the effects on dynamical simulations of core collapse and its neutrino signatures of nucleon-nucleon bremsstrahlung, inelastic neutrino-electron scattering, weak-magnetism/recoil, and artificial decreases in the neutrino-nucleon scattering rates. Our new algorithm for incorporating inelastic scattering explicitly as a source and a sink in the collision term of the Boltzmann equation is both efficient and robust (§B). Furthermore, we have studied the dependence of the collapse dynamics and neutrino signal on variations in the equation of state, as parametrized by Lattimer and Swesty (1991). Surprisingly, the dependence of the salient quantities of collapse on the EOS (again, as parametrized by Lattimer and Swesty) is weak.

We have computed the collapse, bounce, and post-bounce evolution and neutrino signatures for three progenitors: 11, 15, and 20 $M_\odot$. In the process, we have compared key quantities such as core entropy and electron fraction at bounce, peak neutrino breakout luminosity, and the evolution of the neutrino spectra over hundreds of milliseconds with the corresponding quantities in other recent supernova simulations that employ comparably sophisticated algorithms. We evolve most models to several hundred milliseconds after bounce and although all of our models form regions of net neutrino heating behind the shock, none yields an explosion in the first 250 milliseconds.

We have folded our neutrino spectra with the sensitivities and thresholds of several underground neutrino detectors and have focused on those detectors most likely to observe and uniquely identify the electron-neutrino breakout burst. We show that SuperKamiokande, the Sudbury Neutrino Observatory, and the ICARUS detector might all see this important signature of core collapse. We find that the collapse and breakout electron-neutrino signal in these detectors is remarkably similar (see Fig. 22) for all three progenitors considered in this work. The pre-collapse profiles are different in entropy and composition, but the breakout peak is roughly the same in each model. These results are further confirmed in preliminary runs with a 40 $M_\odot$ progenitor.

Figure 22 shows that the event rate due to charged-current capture of $\bar{\nu}_e$ neutrinos on free protons for the 20 $M_\odot$ progenitor (5850 s^{-1}) is more than double that for the 11 $M_\odot$ model (2920 s^{-1}) 175 ms after bounce. The nearly linear rise in $N(<t)$ reflects the fact that the accretion luminosity is roughly constant in this early post-bounce epoch. The difference between the 11 and 20 $M_\odot$ models can be attributed primarily to a difference in $\dot{M}$ (see Fig. 14), which, in turn, is a consequence of the relatively steeper envelope density profile of the lighter progenitor. The behaviors of the density profiles of the 11 $M_\odot$ and 20 $M_\odot$ models roughly bracket those found in the full progenitor model suite of Woosley & Weaver (1995). Hence, we expect that most other progenitors should yield accretion luminosities that produce $\bar{\nu}_e$ signals between those of the 11 $M_\odot$ and 20 $M_\odot$ models in Fig. 22.

APPENDIX

TABULAR NUCLEAR EQUATION OF STATE

We employ the equation of state due to Lattimer & Swesty (1991) (the LSEOS), based on the finite-temperature liquid drop model of nuclei developed in Lattimer et al. (1985). We have constructed an efficient three-dimensional tabular version of this EOS, taking the matter temperature (T), mass density (ρ), and electron fraction (Y_e) as variables. The table consists of 180 equally spaced points in $\log_{10}[\rho \ (\mathrm{g \ cm^{-3}})]$ with $6.4 \leq \log_{10}[\rho \ (\mathrm{g \ cm^{-3}})] \leq 15.1$, 50 equally spaced Y_e planes with $0.05 \leq Y_e \leq 0.51$, and 180 equally spaced zones in $\log_{10}[T \ (\mathrm{MeV})]$. The table is not cubic. For $\log_{10}[\rho \ (\mathrm{g \ cm^{-3}})] = 6.4$, $-0.8 \leq \log_{10}[T \ (\mathrm{MeV})] \leq 1$. At $\log_{10}[\rho \ (\mathrm{g \ cm^{-3}})] = 15.1$,

$0 \leq \log_{10}[T \text{ (MeV)}] \leq 1.6$. We find this range of temperatures and densities sufficient for all calculations we perform. At each point in the table we save the specific internal energy (E), the pressure (P), the entropy per baryon (s), the specific heat at constant volume (C_V), the neutron, proton, alpha particle, and heavy nucleus fractions (X_n, X_p, X_α, X_H, respectively), A and Z/A for the heavy nucleus, the electron chemical potential (μ_e), $\Gamma_s = \partial \ln P / \partial \ln \rho|_s$, $\partial P / \partial T|_\rho$, $\hat{\mu} = \mu_n - \mu_p$, and the derivatives $\partial \hat{\mu} / \partial T$ and $\partial \hat{\mu} / \partial Y_e$. In total, our tabular LSEOS takes up ~ 200 Megabytes of memory. Given T, ρ, and Y_e, the EOS performs three six-point bivariant interpolations (Abromowitz & Stegun 1972) in the $T - \rho$ planes nearest to and bracketing the given Y_e point. A quadratic interpolation is then executed between Y_e points to obtain the desired thermodynamic quantity. This procedure is employed for all quantities in the table except the mass fractions of neutrons, protons, alpha particles, and the heavy nucleus. For these quantities, two four-point bivariant interpolations in the $T - \rho$ plane are combined with a linear interpolation between Y_e planes. The table uses integer arithmetic to find nearest neighbor points, thus alleviating the need for time-intensive search algorithms. Because most hydrodynamics routines update specific internal energy, we include a Newton-Raphson/bisection scheme which iterates on temperature, given a fixed internal energy, until the root is found to within a part in 10^8. Similar iteration routines are employed if one wishes to iterate on entropy or pressure.

The LSEOS extends down to only $\sim 5 \times 10^6$ g cm^{-3} and its validity in this density regime is guaranteed only for fairly high temperatures - the assumption of NSE being thereby satisfied. For calculations in which an explosion occurs, the shock will quickly evolve down the progenitor density gradient to regions where the LSEOS breaks down. For this reason we have coupled to our tabular version of the LSEOS the Helmholtz EOS (Timmes & Arnett 1999; Timmes & Swesty 2000), which contains electrons and positrons at arbitrary degeneracy and relativity, photons, nuclei and nucleons as non-relativistic ideal gases, and Coulomb corrections. At $\rho = 6 \times 10^7$ g cm^{-3} we assume the LSEOS is valid. At $\rho = 4 \times 10^7$ g cm^{-3} we employ only the Helmholtz EOS. For densities between the two, we quadratically interpolate all relevant thermodynamic quantities. Because the LSEOS assumes NSE and the Helmholtz EOS takes non-NSE abundances, there is no thermodynamic consistency between the two EOSs. Fortunately, in thermodynamical regimes relevant for core collapse at these densities, the electron-positron/photon component of the matter dominates the pressure. Therefore, one expects few hydrodynamic artifacts in piecing together these two equations of state. In fact, given a realistic composition for the Helmholtz EOS, at a density of $\rho = 5 \times 10^7$ g cm^{-3}, pressure differences between the LSEOS and Helmholtz EOS are $\sim 1\%$ in the stellar profiles we employ in this study. Differences in entropy, however, are of order 5-10%.

We have performed an extensive set of tests of our tabular implementation of the LSEOS to ensure that thermodynamical consistency is maintained during dynamical simulations. These tests include the adiabatic compression of a single fluid element over eight orders of magnitude (from an initial density of 10^7 g cm^{-3}) and the purely hydrodynamical core collapse of realistic supernova progenitors. For the single-element tests, we use the fractional change in the element entropy ($\Delta s / s_i$, where s_i is the initial entropy at low density) to assess the consistency of the LSEOS as the element is compressed and the density increases to $\sim 5 \times 10^{14}$ g cm^{-3}. For fractional changes in the density (or specific volume) at each step of 1%, our table gives $\Delta s / s_i \sim 0.5\%$. This is to be compared with the results using the actual analytic LSEOS, from which the table was composed, which yield $\Delta s / s_i \sim 0.25\%$. The number of temperature and density points used in the table does effect $\Delta s / s_i$. For example, using just 100 T, 100 ρ, and 50 Y_e points over the same ranges as the larger table raises $\Delta s / s_i$ to about $\sim 1.25\%$. In all our calculations we have opted for the larger table. For the adiabatic collapse tests, we coupled the LSEOS to a variety of one-dimensional hydrodynamics schemes. With radiation turned off and before any shocks form, each mass zone should remain isentropic during the collapse of a massive progenitor star. Using a variety of zoning schemes with both artificial-viscosity and Riemann solvers for shock capturing and resolution, we found that higher-order EOS interpolation schemes as described in Swesty (1996) are not needed to maintain the degree of adiabaticity (1%) during collapse and bounce that we were able to achieve with our more straightforward tabular and interpolation routines.

INELASTIC NEUTRINO SCATTERING

A number of authors have addressed the issue of inelastic neutrino-electron scattering as an important energy redistribution process, which helps thermalize the neutrinos and increases their energetic coupling to the matter in supernova explosions (Bruenn 1985; Mezzacappa & Bruenn 1993). Here, we review the Legendre expansion formalism for approximating the angular dependence of the scattering kernel, and detail our own implementation of scattering terms in the Boltzmann equation.

The general collision integral for inelastic scattering may be written (Bruenn 1985) as

$$\mathcal{L}_\nu^{\text{scatt}}[f_\nu] = (1 - f_\nu) \int \frac{d^3 p'_\nu}{c(2\pi\hbar c)^3} f'_\nu R^{\text{in}}(\varepsilon_\nu, \varepsilon'_\nu, \cos\theta) - f_\nu \int \frac{d^3 p'_\nu}{c(2\pi\hbar c)^3} (1 - f'_\nu) R^{\text{out}}(\varepsilon_\nu, \varepsilon'_\nu, \cos\theta)$$
$$= \tilde{\eta}_\nu^{\text{scatt}} - \tilde{\chi}_\nu^{\text{scatt}} f_\nu \tag{B1}$$

where $\cos\theta$ is the cosine of the scattering angle, ε_ν is the incident neutrino energy, and ε'_ν is the scattered neutrino energy. Although we suppress it here, the incident and scattered neutrino phase space distribution functions (f_ν and f'_ν, respectively) have the following dependencies: $f_\nu = f_\nu(r, t, \mu, \varepsilon_\nu)$ and $f'_\nu = f'_\nu(r, t, \mu', \varepsilon'_\nu)$. μ and μ' are the cosines of the angular coordinate of the zenith angle in spherical symmetry and are related to $\cos\theta$ through

$$\cos\theta = \mu\mu' + [(1 - \mu^2)(1 - \mu'^2)]^{1/2} \cos(\phi - \phi'). \tag{B2}$$

R^{in} is the scattering kernel for scattering **in**to the bin (ε_ν, μ) from any bin (ε'_ν, μ') and R^{out} is the scattering kernel for scattering **out** of the bin (ε_ν, μ) to any bin (ε'_ν, μ'). The kernels are Green functions, correlation functions that connect points in energy and momentum space. In fact, one may also write $R(\varepsilon_\nu, \varepsilon'_\nu, \cos\theta)$ as $R(q, \omega)$, where $\omega(= \varepsilon_\nu - \varepsilon'_\nu)$ is the energy transfer and $q(= [\varepsilon_\nu^2 + \varepsilon'^2_\nu - 2\varepsilon_\nu \varepsilon'_\nu \cos\theta]^{1/2})$ is the momentum transfer, so that the kernel explicitly reflects these dependencies.

It is clear from eq. (B1) that the source, or the net scattering into the beam (ε_ν, μ) is a function of the occupancy (f'_ν) in all other beams. The sink term also depends on f'_ν through the blocking term ($1-f'_\nu$), reflecting the Fermi-Dirac statistics of the neutrino. A solution to the Boltzmann equation yields f_ν (and, hence, f'_ν) at all times, radii, energies, and angles. f_ν is not known a priori and cannot be assumed to be Fermi-Dirac. Only in equilibrium should f_ν approach a Fermi-Dirac distribution, characterized by the local temperature and with a chemical potential that reflects the local neutrino number density. The transport problem is difficult enough without the added complication of non-linear integral source terms. The full implicit solution, including energy and angular redistribution, is numerically cumbersome. Instead, we make several simplifications that make the problem tractable, efficiently solved, and explicit.

An important simplification comes from detailed balance, a consequence of the fact that these scattering rates must drive the distribution to equilibrium; $R^{\mathrm{in}} = e^{-\beta\omega}R^{\mathrm{out}}$, where $\beta = 1/T$. We may therefore deal only with R^{out}. The scattering kernels generally have complicated dependencies on scattering angle and the angular integration over scattered neutrino phase space, implicit in eq. (B1), cannot be computed analytically. For this reason, we approximate the angular dependence of the scattering kernel with a truncated Legendre series (Bruenn 1985). That is, we take

$$R^{\mathrm{out}}(\varepsilon_\nu, \varepsilon'_\nu, \cos\theta) = \sum_{l=0}^{\infty} \frac{2l+1}{2} \Phi(\varepsilon_\nu, \varepsilon'_\nu, \cos\theta) P_l(\cos\theta), \tag{B3}$$

where

$$\Phi_l(\varepsilon_\nu, \varepsilon'_\nu) = \int_{-1}^{+1} d(\cos\theta) R^{\mathrm{out}}(\varepsilon_\nu, \varepsilon'_\nu, \cos\theta) P_l(\cos\theta). \tag{B4}$$

In practice, we expand only to first order so that

$$R^{\mathrm{out}}(\varepsilon_\nu, \varepsilon'_\nu, \cos\theta) \sim \frac{1}{2}\Phi_0(\varepsilon_\nu, \varepsilon'_\nu) + \frac{3}{2}\Phi_1(\varepsilon_\nu, \varepsilon'_\nu)\cos\theta. \tag{B5}$$

Substituting into the first term on the right-hand-side of eq. (B1) (the source) gives

$$\tilde{\eta}_\nu^{\mathrm{scatt}} = (1-f_\nu)\int_0^\infty \frac{d\varepsilon'_\nu \varepsilon'^2_\nu}{c(2\pi\hbar c)^3} e^{-\beta\omega} \int_{-1}^{+1} d\mu' f'_\nu \int_0^{2\pi} d\phi' \left[\frac{1}{2}\Phi_0 + \frac{3}{2}\Phi_1\cos\theta\right] \tag{B6}$$

Substituting for $\cos\theta$ using eq. (B2) and using the definitions

$$\tilde{J}_\nu = \frac{1}{2}\int_{-1}^{+1} d\mu f_\nu \qquad \text{and} \qquad \tilde{H}_\nu = \frac{1}{2}\int_{-1}^{+1} d\mu \mu f_\nu \tag{B7}$$

we have that

$$\tilde{\eta}_\nu^{\mathrm{scatt}} = (1-f_\nu)\frac{4\pi}{c(2\pi\hbar c)^3}\int_0^\infty d\varepsilon'_\nu \varepsilon'^2_\nu e^{-\beta\omega}\left[\frac{1}{2}\Phi_0\tilde{J}'_\nu + \frac{3}{2}\Phi_1\mu\tilde{H}'_\nu\right]. \tag{B8}$$

Integrating over μ to get the source for the zeroth-moment equation,

$$\frac{1}{2}\int_{-1}^{+1} d\mu\,\tilde{\eta}_\nu^{\mathrm{scatt}} = \frac{4\pi}{c(2\pi\hbar c)^3}\int_0^\infty d\varepsilon'_\nu \varepsilon'^2_\nu e^{-\beta\omega}\left[\frac{1}{2}\Phi_0\tilde{J}'_\nu(1-\tilde{J}_\nu) - \frac{3}{2}\Phi_1\tilde{H}_\nu\tilde{H}'_\nu\right]. \tag{B9}$$

Similarly, employing the Legendre expansion, we may write the sink term of the Boltzmann collision integral in terms of the angular moments of f'_ν:

$$\tilde{\chi}_\nu^{\mathrm{scatt}} = \frac{4\pi}{c(2\pi\hbar c)^3}\int_0^\infty d\varepsilon'_\nu \varepsilon'^2_\nu \left[\frac{1}{2}\Phi_0(1-\tilde{J}'_\nu) - \frac{3}{2}\Phi_1\mu\tilde{H}'_\nu\right]. \tag{B10}$$

The contribution to the zeroth-moment equation is then

$$\frac{1}{2}\int_{-1}^{+1} d\mu(-\tilde{\chi}_\nu^{\mathrm{scatt}}f_\nu) = -\frac{4\pi}{c(2\pi\hbar c)^3}\int_0^\infty d\varepsilon'_\nu \varepsilon'^2_\nu \left[\frac{1}{2}\Phi_0(1-\tilde{J}'_\nu)\tilde{J}_\nu - \frac{3}{2}\Phi_1\tilde{H}_\nu\tilde{H}'_\nu\right]. \tag{B11}$$

Combining these equations, we find that

$$\frac{1}{2}\int_{-1}^{+1} d\mu\,\mathcal{L}_\nu^{\mathrm{scatt}}[f_\nu] = \frac{4\pi}{c(2\pi\hbar c)^3}\int_0^\infty d\varepsilon'_\nu \varepsilon'^2_\nu \left\{\frac{1}{2}\Phi_0\left[\tilde{J}'_\nu(1-\tilde{J}_\nu)e^{-\beta\omega} - (1-\tilde{J}'_\nu)\tilde{J}_\nu\right] - \frac{3}{2}\Phi_1\tilde{H}_\nu\tilde{H}'_\nu(e^{-\beta\omega}-1)\right\}. \tag{B12}$$

One can see immediately that including another term in the Legendre expansion, i.e. taking

$$R^{\mathrm{out}} \sim (1/2)\Phi_0 + (3/2)\Phi_1\cos\theta + (5/2)\Phi_2(1/2)(3\cos^2\theta - 1),$$

necessitates including $\tilde{P}_\nu$ and $\tilde{P}'_\nu$, the second angular moment of the neutrino phase-space distribution function, in the source and sink terms. Our transport scheme porvides both the zeroth- and first-moment equations with the spectral Eddington factors $p_\nu = \tilde{P}_\nu/\tilde{J}_\nu$ and $g_\nu = \tilde{N}_\nu/\tilde{J}_\nu$, where

$$\tilde{P}_\nu = \frac{1}{2}\int_{-1}^{+1} d\mu\mu^2 f_\nu \quad \text{and} \quad \tilde{N}_\nu = \frac{1}{2}\int_{-1}^{+1} d\mu\mu^3 f_\nu. \tag{B13}$$

It is therefore straightforward for us to include terms up to $R^{\mathrm{out}} \propto \cos^3\theta$ in our Legendre expansion of the scattering kernel. In practice, however, we retain only the linear term.

Neutrino-Electron Scattering

The scattering kernel $R(\varepsilon_\nu, \varepsilon'_\nu, \cos\theta)$ in §B is related to the fully relativistic structure function for neutrino-electron scattering;

$$R^{\text{out}}(\varepsilon_\nu, \varepsilon'_\nu, \cos\theta) = 2G^2 \frac{q^2_\mu}{\varepsilon'_\nu \varepsilon_\nu}[A\mathcal{S}_1(q,\omega) + \mathcal{S}_2(q,\omega) + B\mathcal{S}_3(q,\omega)](1 - e^{-\beta\omega})^{-1}. \tag{B14}$$

The relativistic structure functions ($\mathcal{S}_i$) are given in terms of the imaginary part of the polarization functions (Π). Each of the retarded polarization functions can be written in terms of one-dimensional integrals over electron energy (ε_e) (see Reddy, Prakash, & Lattimer 1998).

Even though we have made the simplifying assumption that the scattering kernel can be approximated by a Legendre series truncated at first order (eq. B5), in a fully dynamical calculation it is numerically costly to compute the Legendre moments of the scattering kernel ($\Phi_0(\varepsilon_\nu, \varepsilon'_\nu)$ and $\Phi_1(\varepsilon_\nu, \varepsilon'_\nu)$) via eq. (B4) at each point on the radial grid (at each temperature, density, and composition point) at each time step. In order to decrease the computation time, we tabulate $\Phi_0(\varepsilon_\nu, \varepsilon'_\nu)$ and $\Phi_1(\varepsilon_\nu, \varepsilon'_\nu)$ for each ε_ν and ε'_ν, for each neutrino species, on a grid in temperature and η_e. At each T-η_e point, we calculate both kernels for each ε_ν-ε'_ν point, given the energy grouping for the particular calculation. The angular integrals over $\cos\theta$ for $l = 0$ and $l = 1$ in eq. (B4) are carried out using 16-point Gauss-Legendre quadratures. During an actual supernova calculation, we use simple trapezoidal rule quadrature to calculate the integral over ε'_ν for a given ε_ν. Each term in this integral contains the kernels, which must be evaluated for each ε_ν-ε'_ν pair at the temperature/density/composition point currently being addressed. η_e is calculated by the equation of state and we do a six-point bivariant interpolation in T-η_e space, for the given ε_ν-ε'_ν combination. In practice, we use 40 energy groups (n_f), 30 temperature points (N_T), and 30 η_e points (N_η). The tables are then $l \times n_f \times n'_f \times N_T \times N_\eta$ in size, with $l = 2$ (Φ_0 and Φ_1), or approximately 50 Megabytes. Since the vector and axial-vector couplings for electron scattering are different for each neutrino species, we compute tables for ν_e, $\bar{\nu}_e$, and ν_μ for each dynamical calculation. $\tilde{\eta}^{\text{scatt}}_\nu$ and $\tilde{\chi}^{\text{scatt}}_\nu$ are then included explicitly as a source and sink, respectively, in a manner analogous to any of the absorption and emission processes detailed in Burrows (2001). Using this method, our calculations including neutrino-electron scattering, are just 10-15% slower than our calculations ignoring this important equilibration process.

Because we do not evaluate the scattering source and sink implicitly, we introduce an explicit timescale into the energy and electron fraction updates returned by our transport algorithm. In effect, if the scattering timescale $(c\tilde{\chi}^{\text{scatt}}_\nu)^{-1}$ is shorter than our timestep, we may encounter a numerical instability. For this reason, at high densities, where the neutrino phase-space distribution function is in local thermodynamic equilibrium, we divide the source and sink by a factor (typically 100 above $\rho = 10^{14}$ g cm^{-3}). This reduces the rate artificially, thus increasing the timescale for scattering. As this process is totally negligible in this regime, particularly considering the fact that $f_\nu = f^{\text{eq}}_\nu$ at these high densities, this approximation is acceptable.

REFERENCES

Abromowitz, M. & Stegun, I. A., *Handbook of Mathematical Functions* (Dover Publications, Inc., New York, 1972)
Ahmad et al. (2002), SNO collaboration, Phys. Rev. Lett., 89, 011301
Ando, S. & Sato, K. 2002, Progress of Theoretical Physics, 107, 957
Beacom, J. F., Boyd, R. N., & Vogel, P. 2000, Phys. Rev. Lett., 85, 3568
Beacom, J. F. & Vogel, P. 1998, Phys. Rev. D, 58, 053010
Bethe, H. & Wilson, J. R. 1985, ApJ, 295, 14
Bhattacharya, M., Garcia, I., Kaloskamis, N. I., Adelberger, E. G., Swanson, H. E., Anne, R., Lewitowicz, M., Saint-Laurent, M. G., Donzaud, C., Guillemand-Mueller, D., Leenhardt, S., Mueller, A. C., Pougheon, F., Sorlin, O., Trinder, W. 1998, Phys. Rev. C, 58, 3677
Bruenn, S. W. 1985, ApJS, 58, 771
Bruenn, S. W., De Nisco, K. R., & Mezzacappa, A. 2001, ApJ, 560, 326
Burrows, A., Klein, D., & Gandhi, R. 1992, Phys. Rev. D, 45, 10, 3361
Burrows, A., Hayes, J., & Fryxell, B. A. 1995, ApJ, 450, 830
Burrows, A., Young, T., Pinto, P., Eastman, R., & Thompson, T. A. 2000, ApJ, 539, 865
Burrows, A. & Sawyer, R. 1998, Phys. Rev. C, 58, 554
Burrows, A. & Sawyer, R. 1999, Phys. Rev. C, 59, 510
Burrows, A. & Lattimer, J.M. 1983, ApJ, 270, 735
Burrows, A. & Lattimer, J.M. 1986, ApJ, 307, 178
Burrows, A. 1988, ApJ, 334, 891
Burrows, A., 2001, Progress in Particle and Nuclear Physics, 46, 59
Dutta, G., Indumathi, D., Murthy, M. V. N., & Rajasekaran, G. 1999, PRD, 61, 013009
Dighe, A. S. & Smirnov, A. Yu. 2000, PRD, 62, 033007
Eastman, R. & Pinto, P. 1993, ApJ, 412, 731
Eguchi, K. et al. 2003, PRL, 90, 021802
Fryer, C. L., Benz, W., Herant, M., & Colgate, S. 1999, ApJ, 516, 892
Fryer, C. L. & Heger, A. 2000, ApJ, 541, 1033
Herant, M., Benz, W., Hix, W. R., Fryer, C. L., Colgate, S. A. 1994, ApJ, 435, 339
Horowitz, C. J. 1997, Phys. Rev. D, 55, 4577
Horowitz, C. J. 2002, Phys Rev. D, 65, 043001
ICARUS collaboration 2001, *The ICARUS Experiment*, Laboratory Nazionali del Gran Sasso, LNGS-P28, (hep-ex/0103008)
Keil, W., Janka, H.-Th., & Müller, E. 1996, ApJ, 473, L111
Janka, H.-Th., Keil, W., Raffelt, G., & Seckel, D. 1996, PRL, 76, 2621

Janka, H.-Th. 2001, A&A, 368, 527
Lattimer, J. M., Pethick, C., Ravenhall, D., & Lamb, D. 1985, Nucl. Phys. A, 432, 646
Lattimer, J. M. & Swesty, F. D. 1991, Nucl. Phys. A, 535, 331
Liebendörfer, M. 2000, Ph.D. Thesis, Basel University, Basel, Switzerland
Liebendörfer, M., Mezzacappa, A., Thielemann, F.-K., Messer, O. E. B., Hix, W. R., & Bruenn, S. W. 2001a, PRD, 63, 103004
Liebendörfer, M., Mezzacappa, A., Thielemann, F.-K. 2001b, PRD, 63, 104003
Liebendörfer, M., Messer, O. E. B., Mezzacappa, A., Hix, W. R., Thielemann, F.-K., & Langanke, K. 2002a, *Proceedings of the 11th Workshop on Nuclear Astrophysics*, Hillebrandt, W. & Müller, E., eds., (astro-ph/0203260)
Liebendörfer, M., Messer, O. E. B., Mezzacappa, A., Cardall, C. Y., & Thielemann, F.-K. 2002b, submitted to ApJS, (astro-ph/0207036)
Loreti, F. N., Qian, Y.-Z., Fuller, G. M., and Balantekin, A. B. 1995, Phys. Rev. D, 52, 6664
Mezzacappa, A. & Bruenn, S. W. 1993a, ApJ, 410, 637
Mezzacappa, A. & Bruenn, S. W. 1993b, ApJ, 410, 669
Mezzacappa, A. & Bruenn, S. W. 1993c, ApJ, 410, 740
Mezzacappa, A., Liebendörfer, M., Messer, O. E. B., Hix, W. R., Thielemann, F.-K., & Bruenn, S. W. 2001, PRL, 86, 1935
Mihalas, D. & Mihalas, B., *Foundations of Radiation Hydrodynamics*, New York, Oxford University Press, 1984
Ormand, W. E., Pizzochero, P. M., Bortignon, R. A., Broglia, R. A. 1995, Phys. Lett. B, 345, 343
Raffelt, G. & Seckel, D. 1998, Phys. Rev. Lett., 69, 2605
Raffelt, G. 2001, ApJ, 561,890
Raghavan, R. S. 1986, Phys. Rev. D, 34, 2088
Rampp, M. 2000, Ph.D. Thesis, Max-Planck Institute for Astrophysics, Garching, Germany.
Rampp, M. & Janka, H.-Th. 2000, ApJL, 539, 33
Rampp, M., Buras, R., Janka, H.-Th., & Raffelt, G. G. 2002, *Proceedings of the 11th Workshop on Nuclear Astrophysics*, Hillebrandt, W. & Müller, E., eds., (astro-ph/0203493)
Rampp, M. & Janka, H.-Th. 2002, submitted to A&A, (astro-ph/0203101)
Reddy, S., Prakash, M., & Lattimer, J. M. 1998, PRD, 58, 013009
Sehgal, I. 1974, Nucl.Phys., B70, 61
Swesty, F. D. 1996, J. Comp. Phys., 127, 118
Takahashi, K., Watanabe, M., Sato, K., & Totani, T. 2001, PRD, 64, 093004

Thompson, T. A., Burrows, A., & Horvath, J. E. 2000, PRC, 62, 035802
Thompson, T. A., Burrows, A., & Meyer, B. S. 2001, ApJ, 562, 887
Timmes, F. X. & Swesty, F. D. 2000, ApJS, 126, 501
Timmes, F. X. & Arnett, D. 1999, ApJS, 125, 277

Totani, T., Sato, K., Dalhed, H. E. & Wilson, J. R. 1998, ApJ, 496, 216
Vogel, P. 1984, Phys. Rev. D, 29, 1918
Vogel, P. & Beacom, J. 1999, PRD, 60, 053003
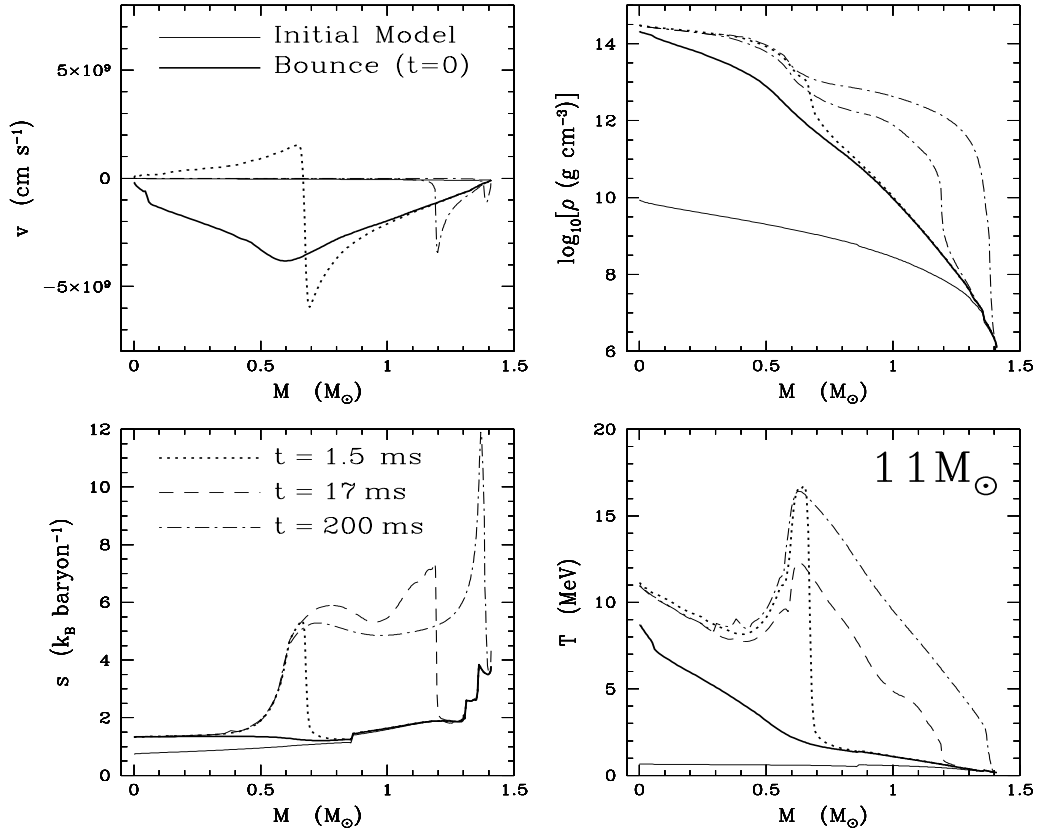Woosley, S. E. & Weaver, T. A. 1995, ApJS, 101, 181

FIG. 1.— Velocity v (in cm s^{-1}, upper left panel), $\log_{10}[\rho]$ (in g cm^{-3}, upper right panel), entropy s (in k$_B$ baryon^{-1}, lower left panel), and temperature T (in MeV, lower right panel) in the 11M$_\odot$ progenitor, as a function of mass coordinate in M$_\odot$ for five snapshots in time. The thin solid line shows the initial configuration and the thick solid line shows the model at bounce. The dotted, dashed, and dot-dashed lines are snapshots at 1.5 ms, 17 ms, and 200 ms after bounce, respectively.
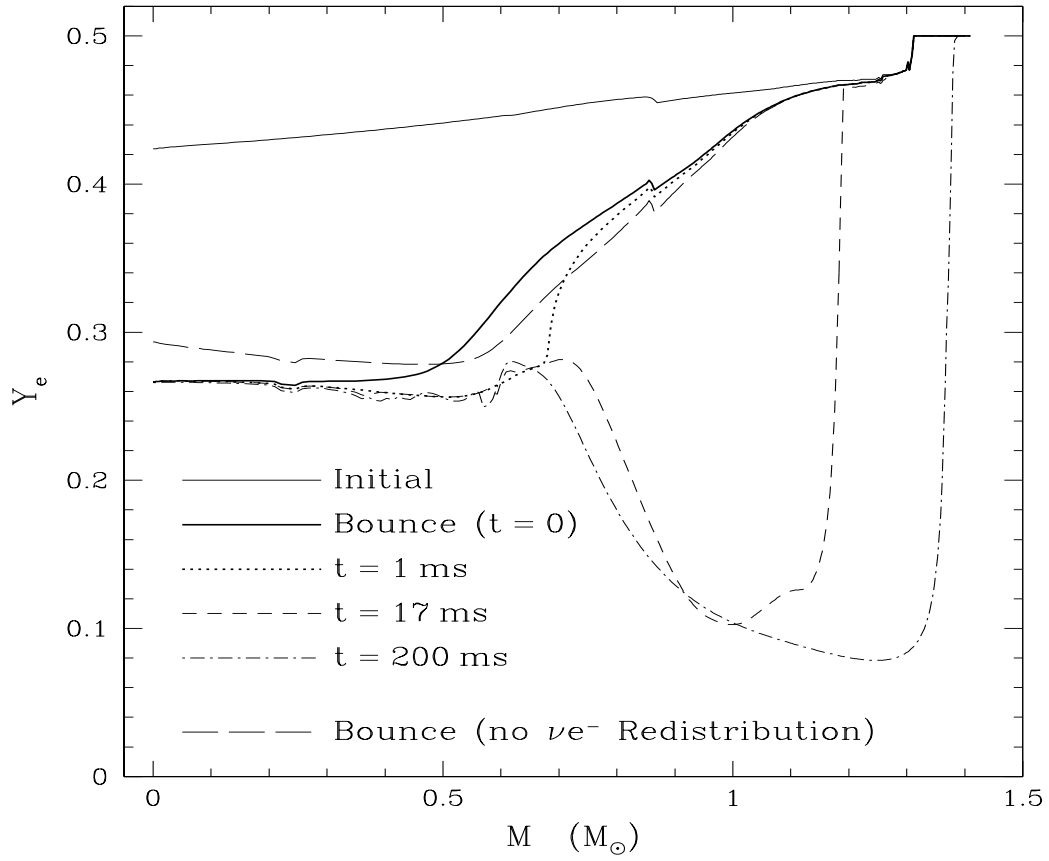
FIG. 2.— The electron fraction Y_e in the $11M_\odot$ progenitor, as a function of mass coordinate in $M_\odot$ for five snapshots in time. The thin solid line shows the initial configuration and the thick solid line shows the model at bounce. The dotted, short-dashed, and dot-dashed lines are snapshots at 1 ms, 17 ms, and 200 ms after bounce, respectively. For comparison, we include the bounce Y_e profile with inelastic neutrino-electron redistribution turned off (long dashed line). Compare this figure with Fig. 1, which shows the basic hydrodynamical evolution for this same model.
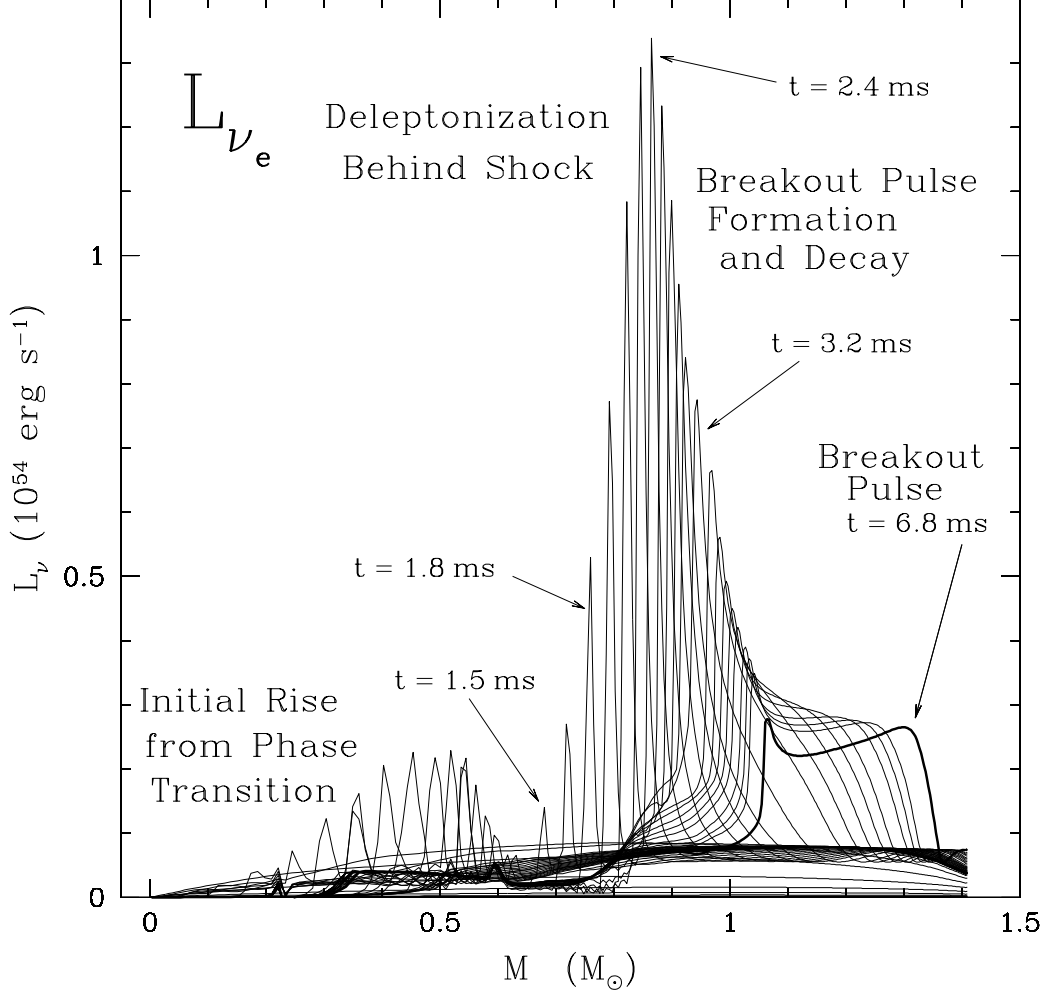
FIG. 3.— Snapshots of L_{ν_e} in 10^{54} erg s^{-1} as a function of mass for the fiducial $11\,M_\odot$ progenitor, showing the whole envelope of luminosities realized in this progenitor from bounce through electron-neutrino breakout. Times re relative to hydrodynamical bounce. The initial rise in L_{ν_e} at $\sim 0.3\,M_\odot$ comes from electron capture on newly liberated free protons before the shock forms, but just after bounce. The second, larger peak forms after shock formation. The temperature and density increase across the shock dissociates nuclei into free nucleons. Subsequent electron capture on free protons generates the breakout pulse, which reaches $L_{\nu_e} \sim 1.5 \times 10^{54}$ erg s^{-1} locally.
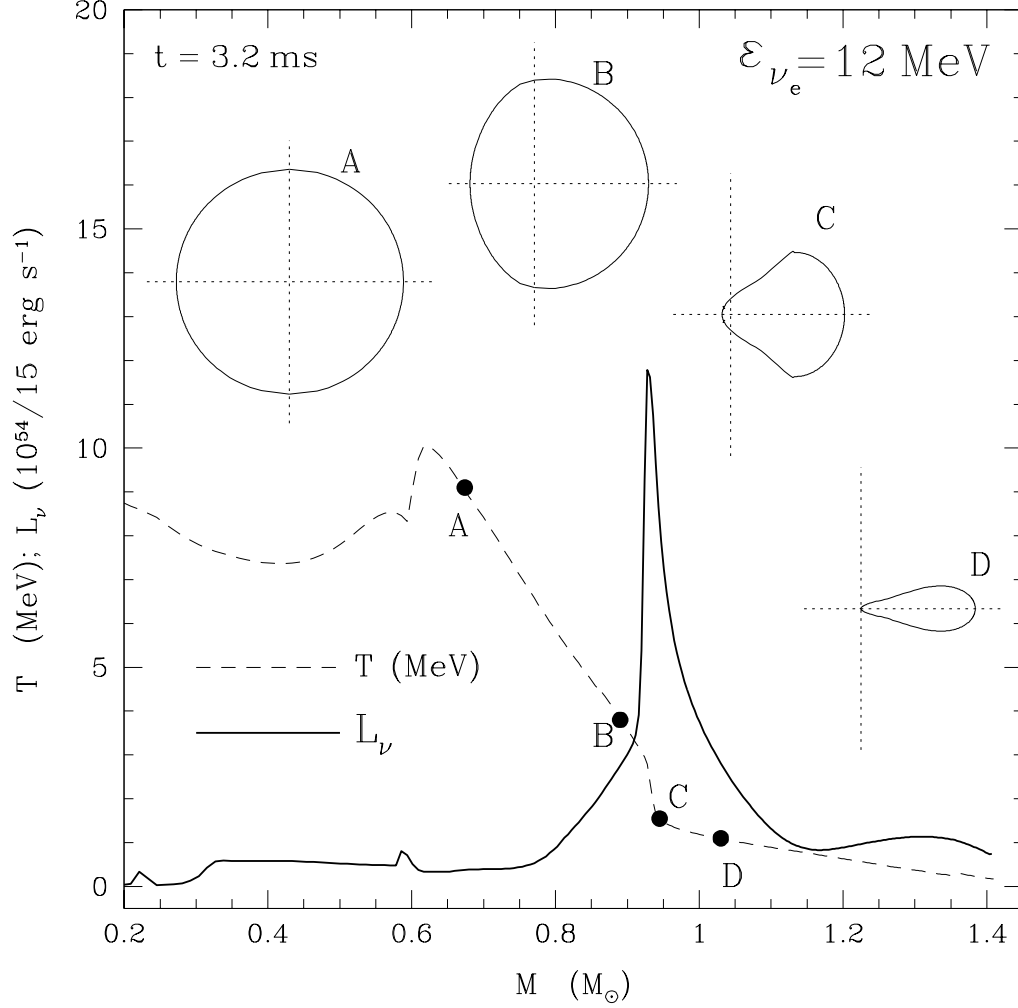
FIG. 4.— Temperature (MeV, dashed line) and electron neutrino luminosity ($10^{54}/15$ erg s^{-1}, thick solid line) as a function of enclosed mass 3.2 ms after bounce. The four small insets (thin solid lines on dotted axes) are polar plots of the angular distribution of the electron-neutrino specific intensity (i.e., $I_\nu(\theta)$) for $\varepsilon_{\nu_e} = 12$ MeV at four mass points: (A) 0.674 $M_\odot$, (B) 0.89 $M_\odot$, (C) 0.945 $M_\odot$, and (D) 1.03 $M_\odot$, each point indicated specifically by large dots on the temperature profile. At (A), the radiation field is isotropic, indicating that the flux is zero and that the neutrinos are trapped. At (D), the radiation field is nearly decoupled from the matter, as indicated by the forward-peaked angular profile.
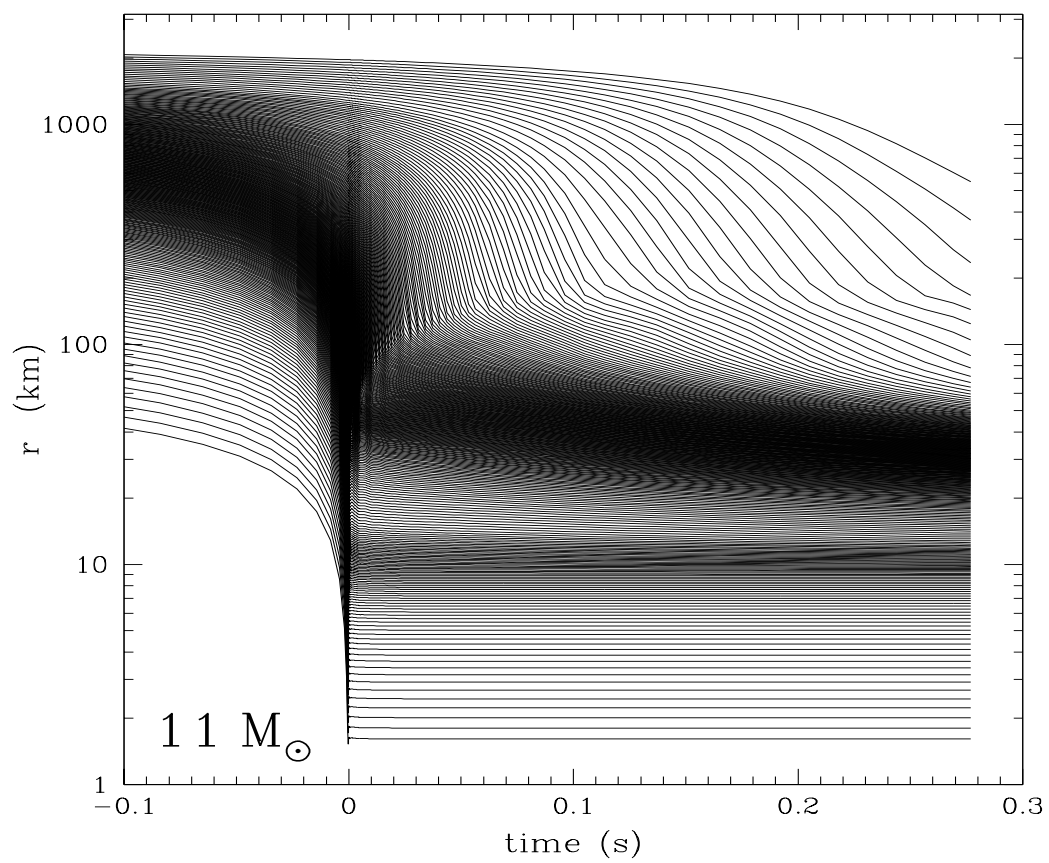
FIG. 5.— The radial position (in km) of selected mass shells as a function of time in our fiducial $11M_\odot$ model.
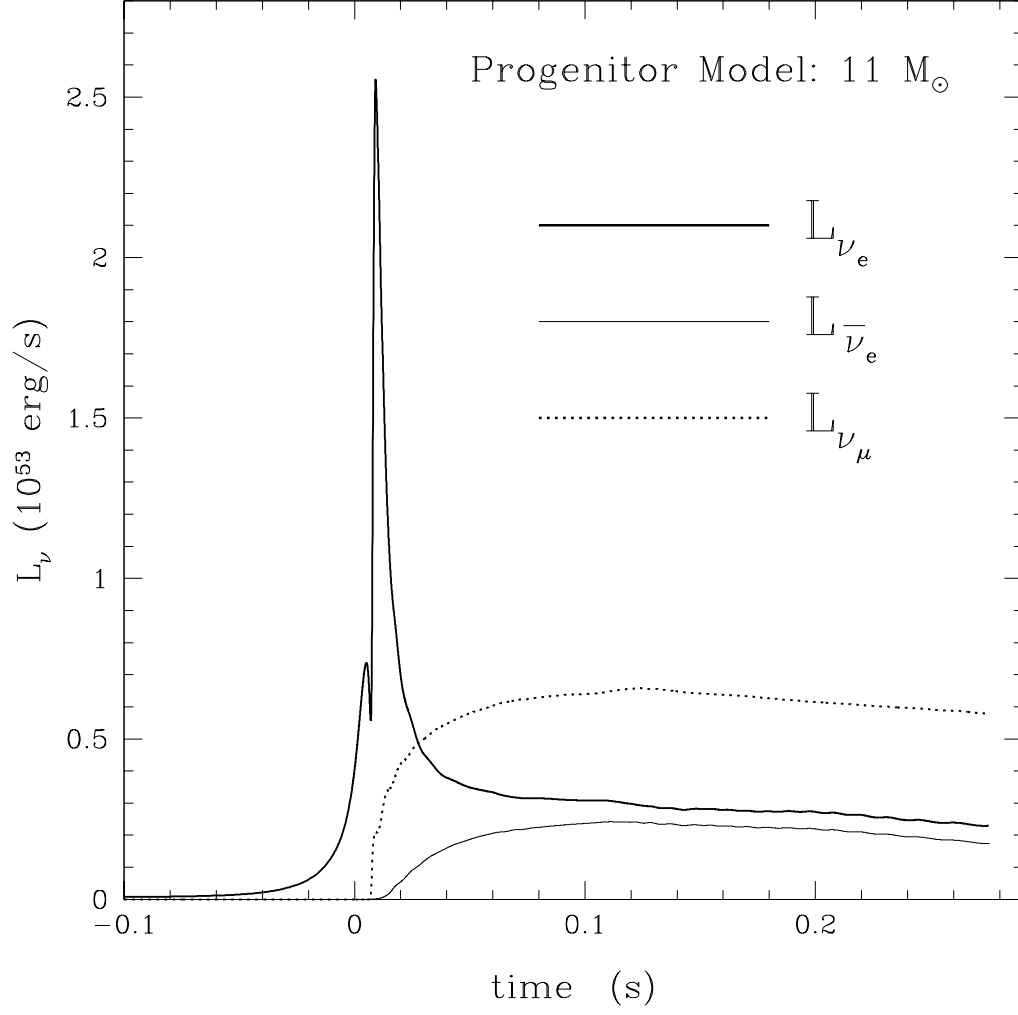
FIG. 6.— L_{ν_e} (thick solid line), $L_{\bar{\nu}_e}$ (thin solid line), and L_{ν_μ} (dotted line) measured at the outer edge of the grid in erg s^{-1} as a function of time for the fiducial M= 11 M$_\odot$ progenitor. Time is measured relative to bounce. Note that we define $t = 0$ as the time of hydrodynamical bounce. The finite light travel-time to the edge of the grid creates a ~ 7 ms offset between hydrodynamical bounce and the initial dip before the large ν_e breakout pulse.
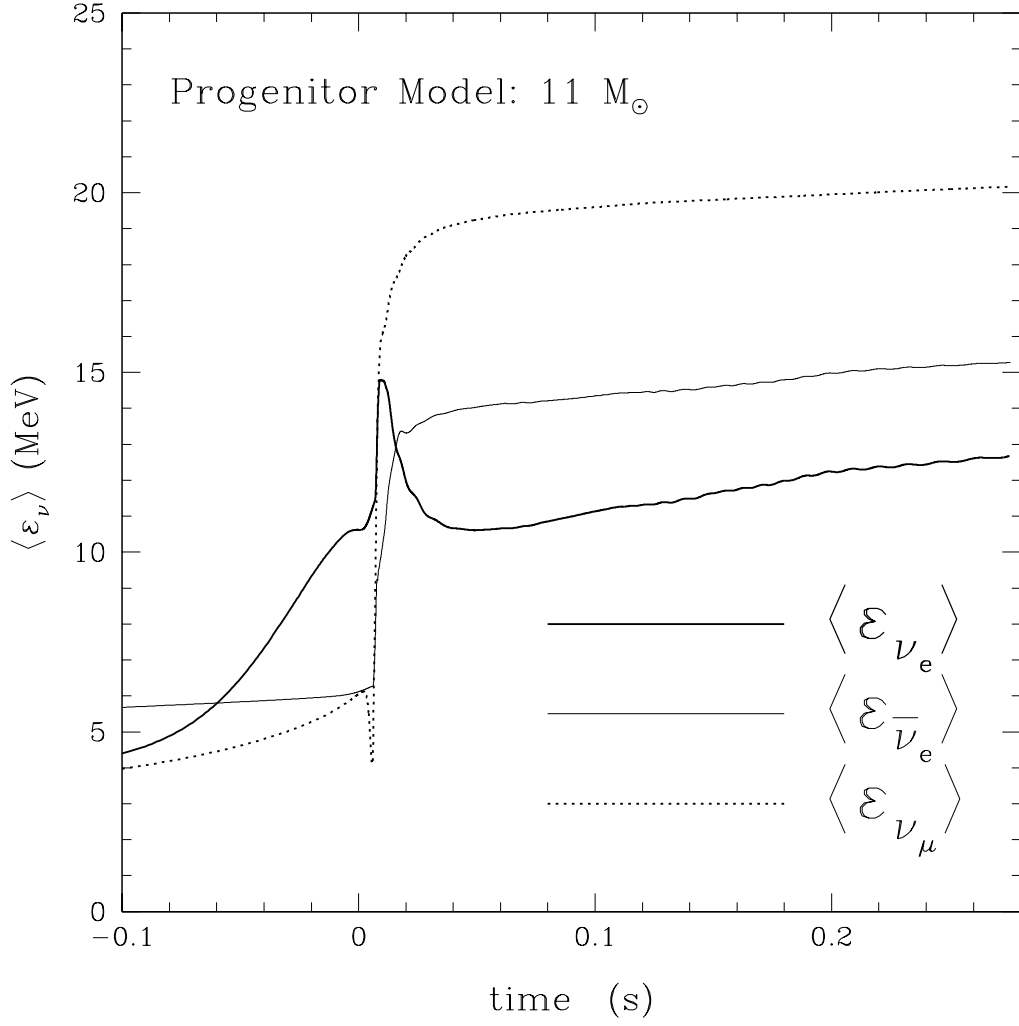
FIG. 7.— $\langle \varepsilon_{\nu_e} \rangle$ (thick solid line), $\langle \varepsilon_{\bar{\nu}_e} \rangle$ (thin solid line), and $\langle \varepsilon_{\nu_\mu} \rangle$ (dotted line) at the outer edge of the grid in MeV as a function of time for the fiducial M= 11 $M_\odot$ progenitor. Averages are computed using eq. (2). Compare with Fig. 6, which shows the corresponding luminosities: L_{ν_e}, $L_{\bar{\nu}_e}$, and L_{ν_μ}.
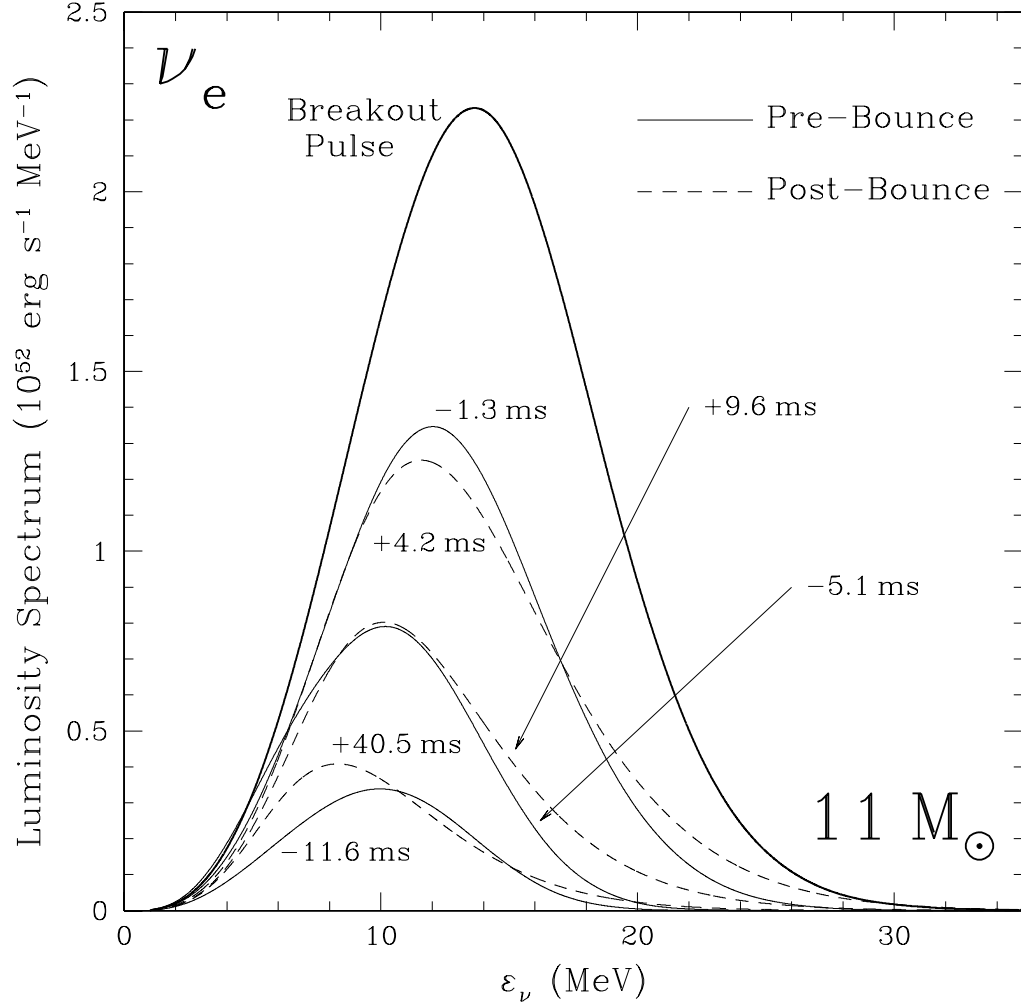
FIG. 8.— Luminosity spectrum of ν_e neutrinos at infinity at various pre- (thin solid lines) and post-breakout (dashed lines) times. In this figure, time is measured relative to the peak breakout spectrum (thick solid line). The thin solid lines correspond to 11.6, 5.1, and 1.3 ms before the peak and the dashed lines denote the ν_e spectrum 4.2, 9.6, and 40.5 ms after the peak.
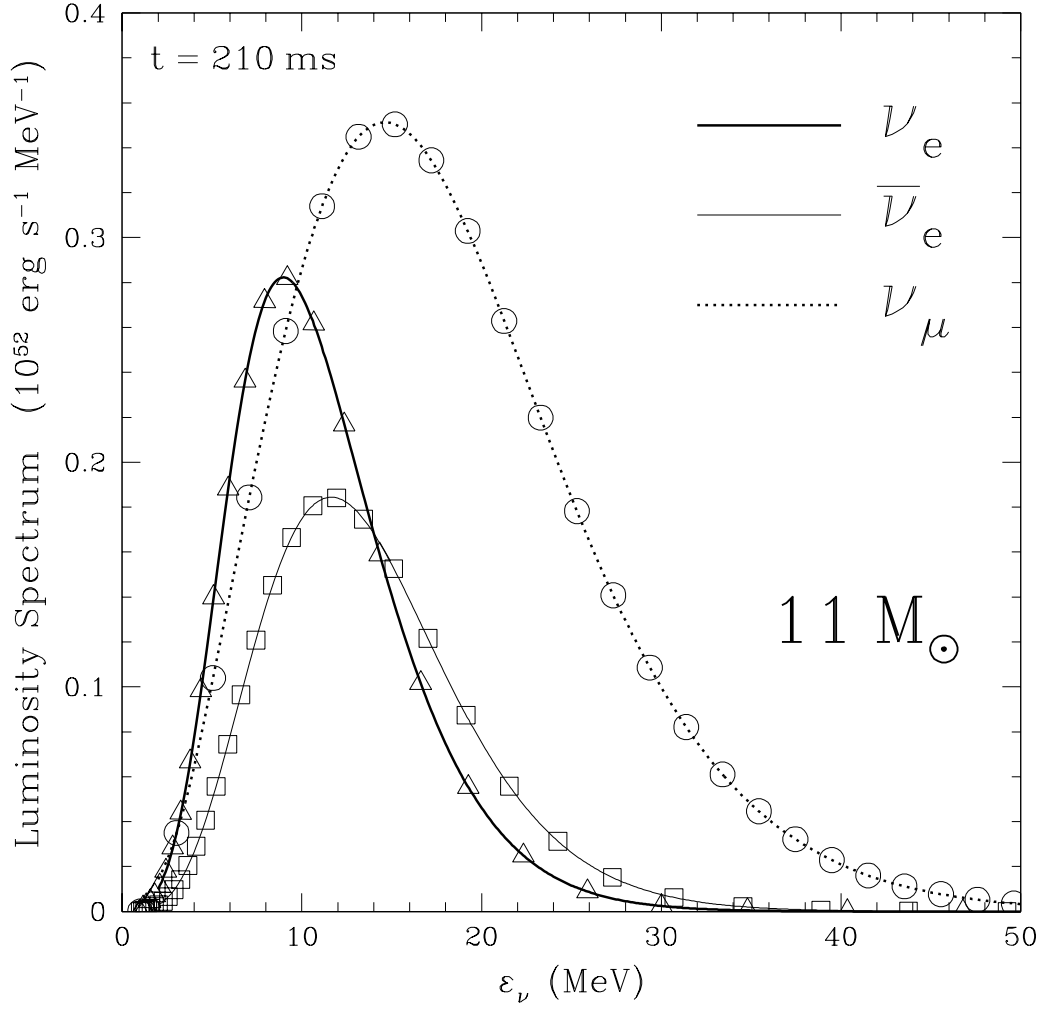
FIG. 9.— Luminosity spectrum of ν_e (thick solid line), $\bar{\nu}_e$ (thin solid line), and ν_μ neutrinos (dotted line) at infinity at $t = 210$ ms after bounce. The actual energy groups are denoted by triangles, squares, and circles for ν_e, $\bar{\nu}_e$, and ν_μ neutrinos, respectively.
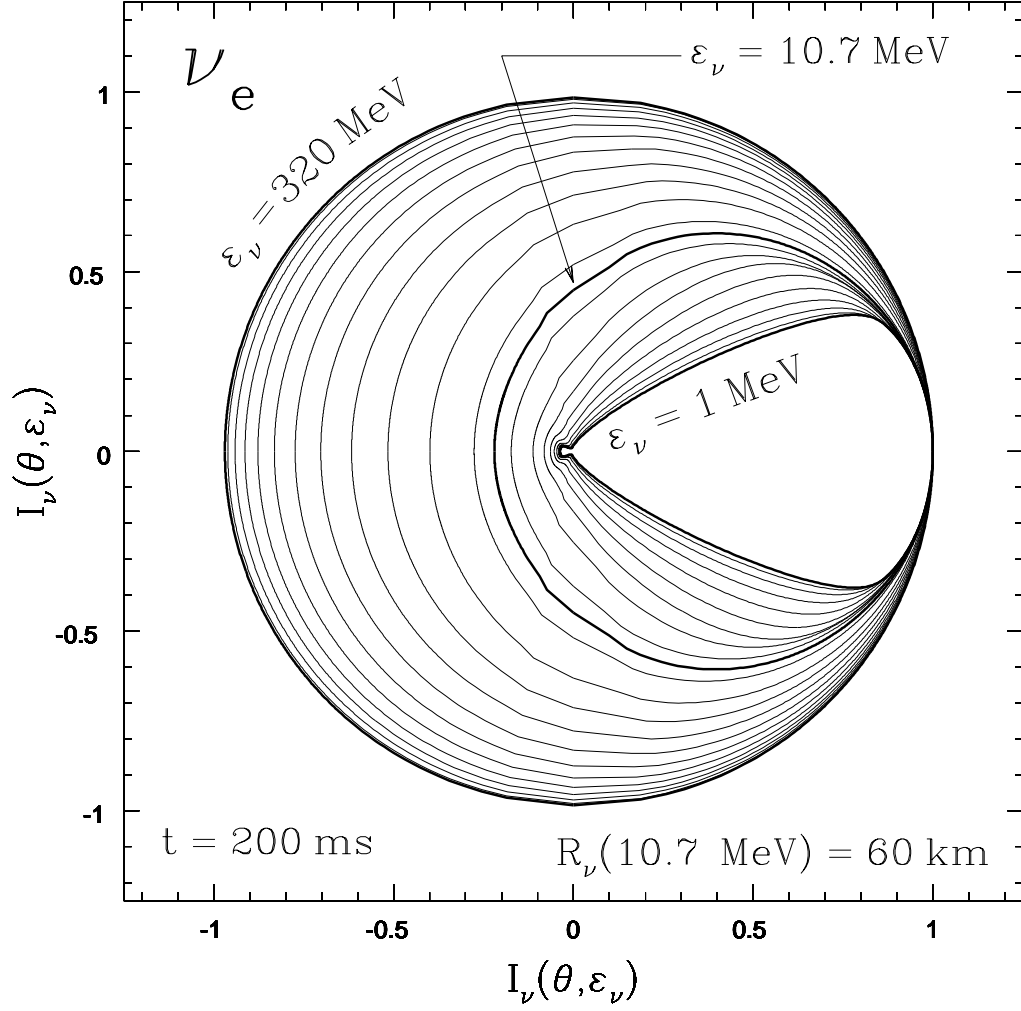
FIG. 10.— Polar plot of the normalized specific intensity, constructed from the Feautrier variables at the neutrinosphere (as defined in eq. 1) for $\varepsilon_\nu \simeq 10.7$ MeV for ν_e neutrinos. This plot shows only every other energy grid point (solid lines). There are 269 angular bins in each quadrant. At the largest energies, the radiation field is nearly isotropic and the flux is quite small. At the lowest energies, the radiation field is beginning to decouple from the matter and I_ν is forward-peaked.
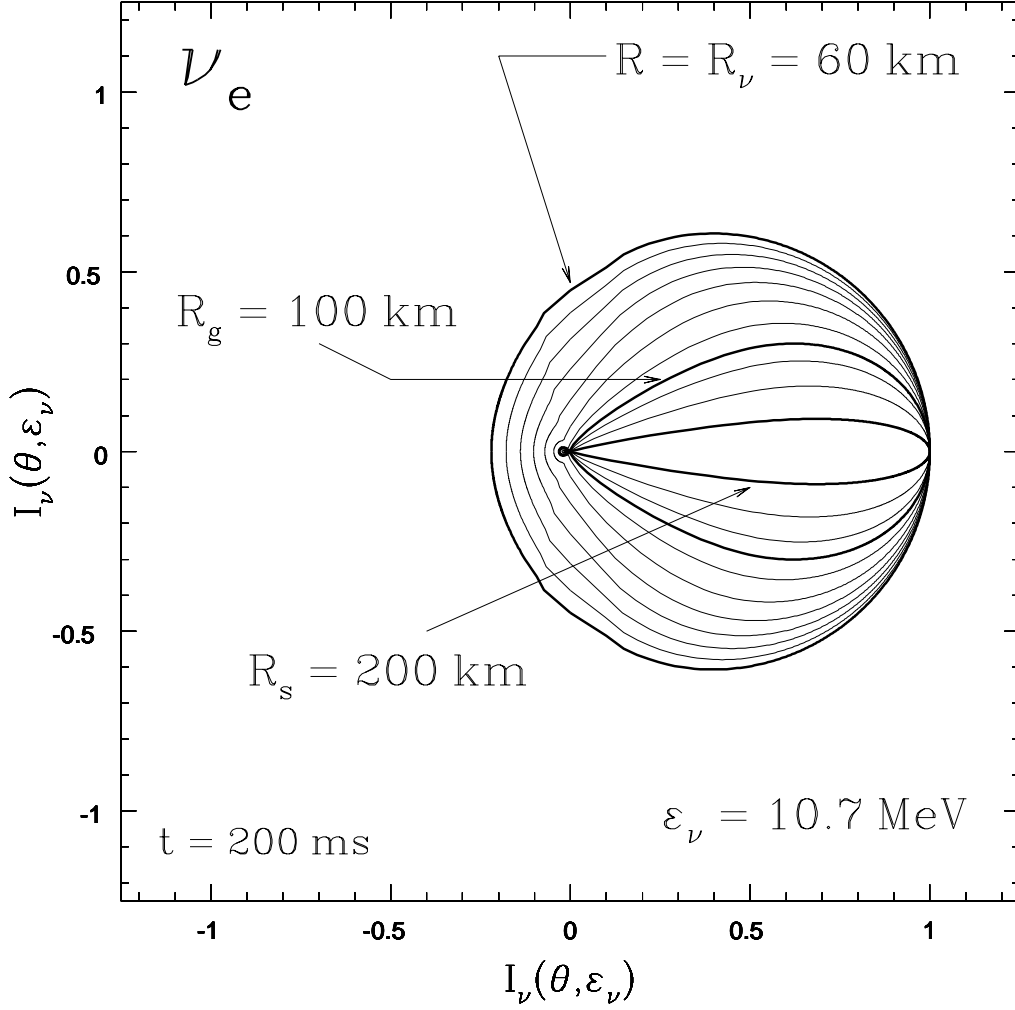
FIG. 11.— Polar plot of the specific intensity (I_{ν_e}) as a function of θ for ν_e neutrinos with $\varepsilon_\nu = 10.7$ MeV at selected radii. We maintain the same scale as in Fig. 10 for the line labeled '60 km' and normalize the absolute value I_ν for all other radii to that reference I_ν. Thick solid lines denote $I_{\nu_e}(\theta, \varepsilon_\nu = 10.7\,\text{MeV})$ at the neutrinosphere ($R_\nu \simeq 60\,\text{km}$), at the gain radius ($R_g \simeq 100\,\text{km}$), and at the shock radius ($R_s \simeq 200\,\text{km}$) 200 ms after bounce. Thin solid lines show the specific intensity at various intermediate radii.
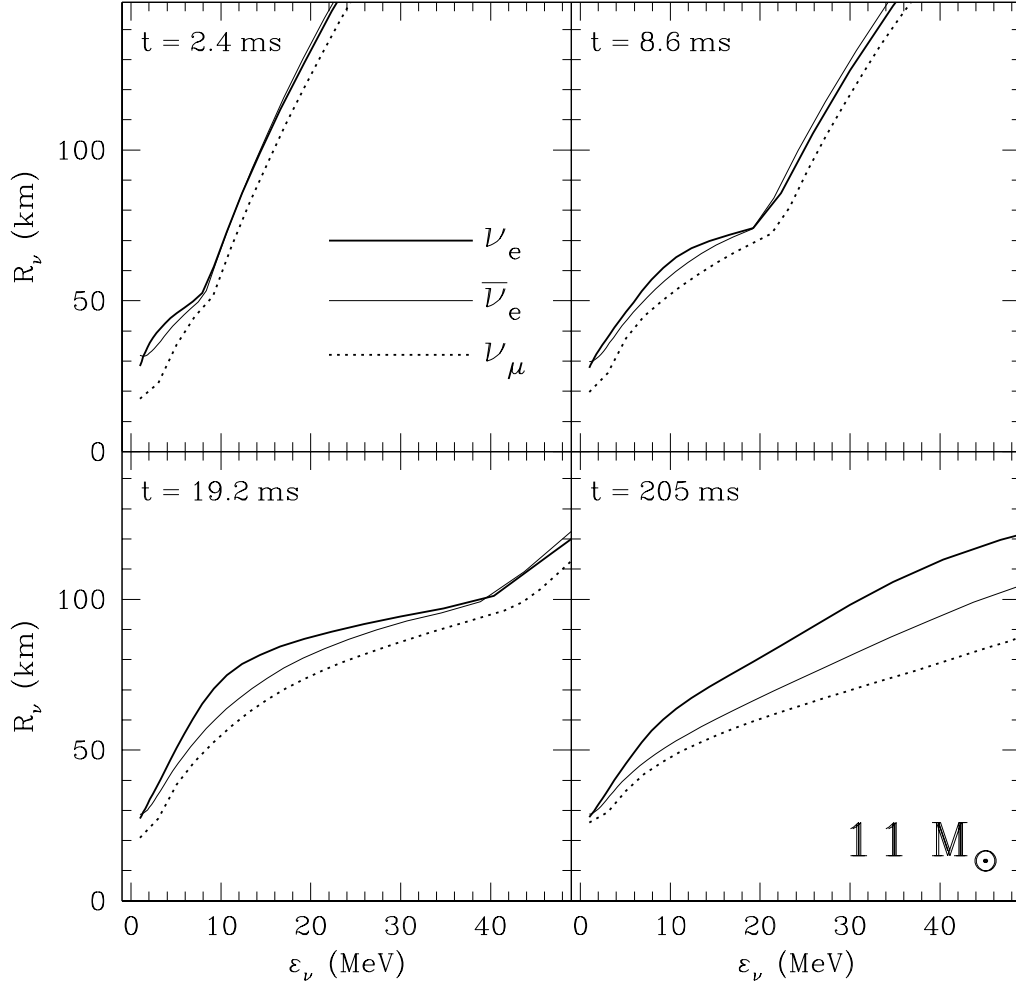
FIG. 12.— The neutrinospheres (as defined by eq. 1) as a function of neutrino energy for each neutrino species (ν_e, thick solid line; $\bar{\nu}_e$, thin solid line; ν_μ, dotted line) for four post-bounce times in the baseline 11 $M_\odot$ model.
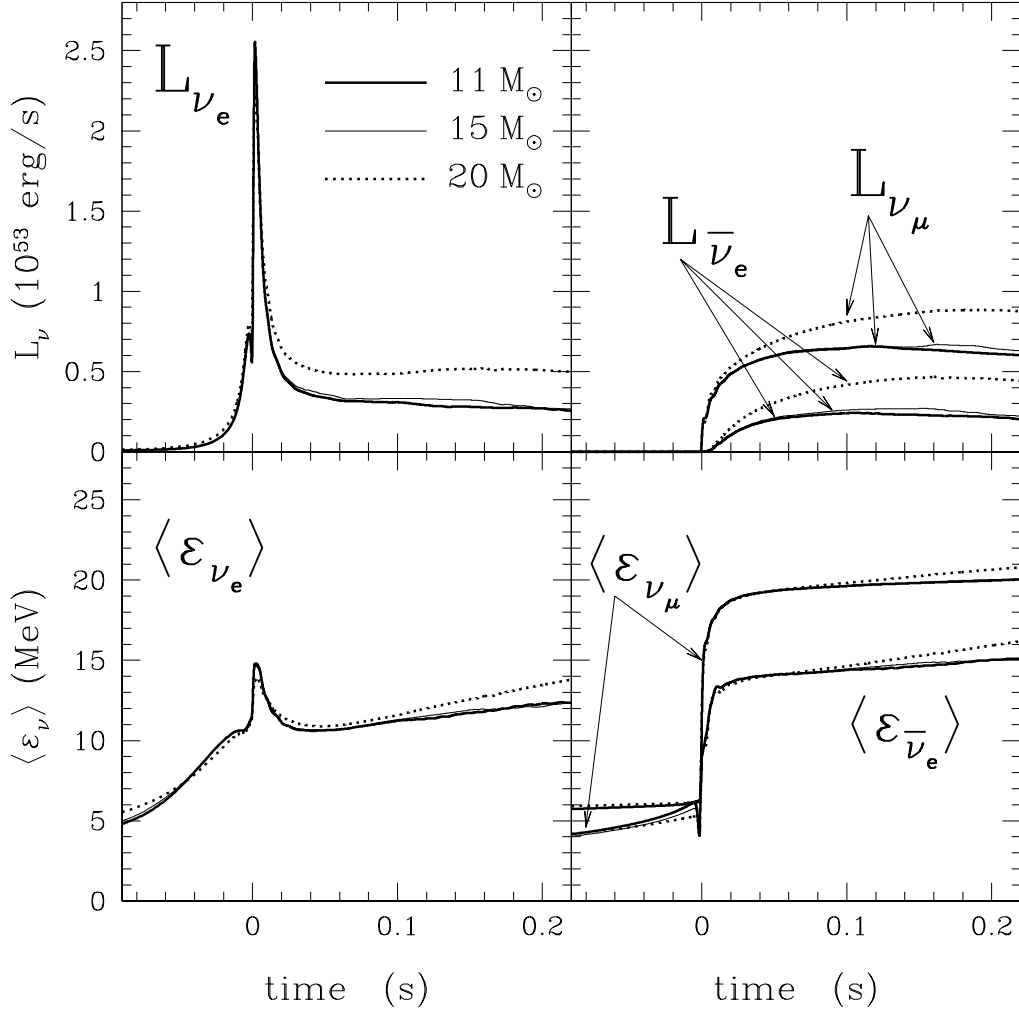
FIG. 13.— L_{ν_e} (10^{53} erg s^{-1}, upper left-hand panel), $L_{\bar{\nu}_e}$ and L_{ν_μ} (upper right-hand panel), $\langle \varepsilon_{\nu_e} \rangle$ (MeV, lower left-hand panel), and $\langle \varepsilon_{\bar{\nu}_e} \rangle$ and $\langle \varepsilon_{\nu_\mu} \rangle$ (lower right-hand panel) as a function of time at infinity for three different progenitors: 11 M$_\odot$ (the baseline model, thick solid line), 15 M$_\odot$ (thin solid line), and 20 M$_\odot$ (dotted line).
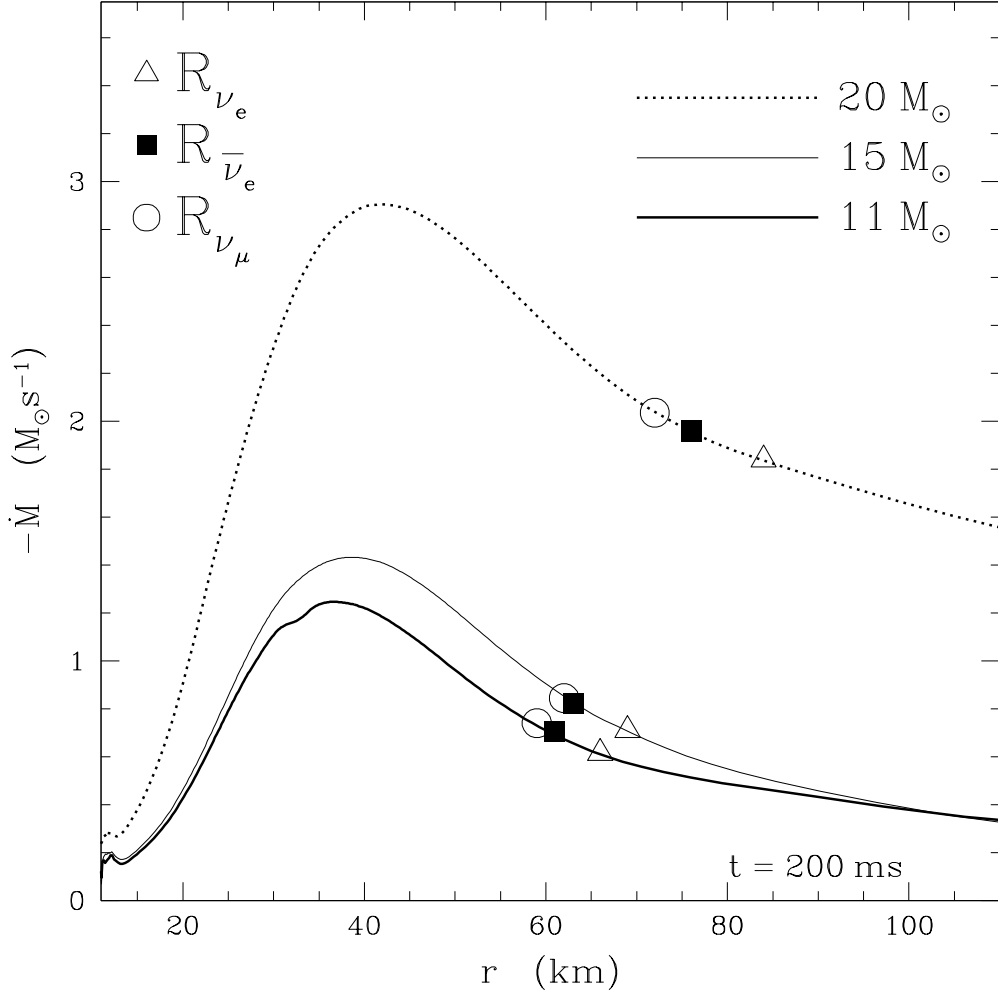
FIG. 14.— Mass flux $\dot{M}$ in $M_\odot$ s^{-1} as a function of radius for our 11 $M_\odot$ (thick solid line), 15 $M_\odot$ (thin solid line), and 20 $M_\odot$ (dotted line) models, all at 200 ms after bounce. Open triangles mark the ν_e neutrinosphere (R_{ν_e}) at $\langle \varepsilon_{\nu_e} \rangle \simeq 12$, 12, and 13.5 MeV for the 11$M_\odot$, 15$M_\odot$, and 20$M_\odot$ models, respectively. Filled squares and open circles mark $R_{\bar{\nu}_e}(\langle \varepsilon_{\bar{\nu}_e} \rangle \simeq 15, 15, 16\,\text{MeV})$ and $R_{\nu_\mu}(\langle \varepsilon_{\nu_\mu} \rangle \simeq 20, 20, 21\,\text{MeV})$ for the 11 $M_\odot$, 15 $M_\odot$, and 20 $M_\odot$ models, respectively.
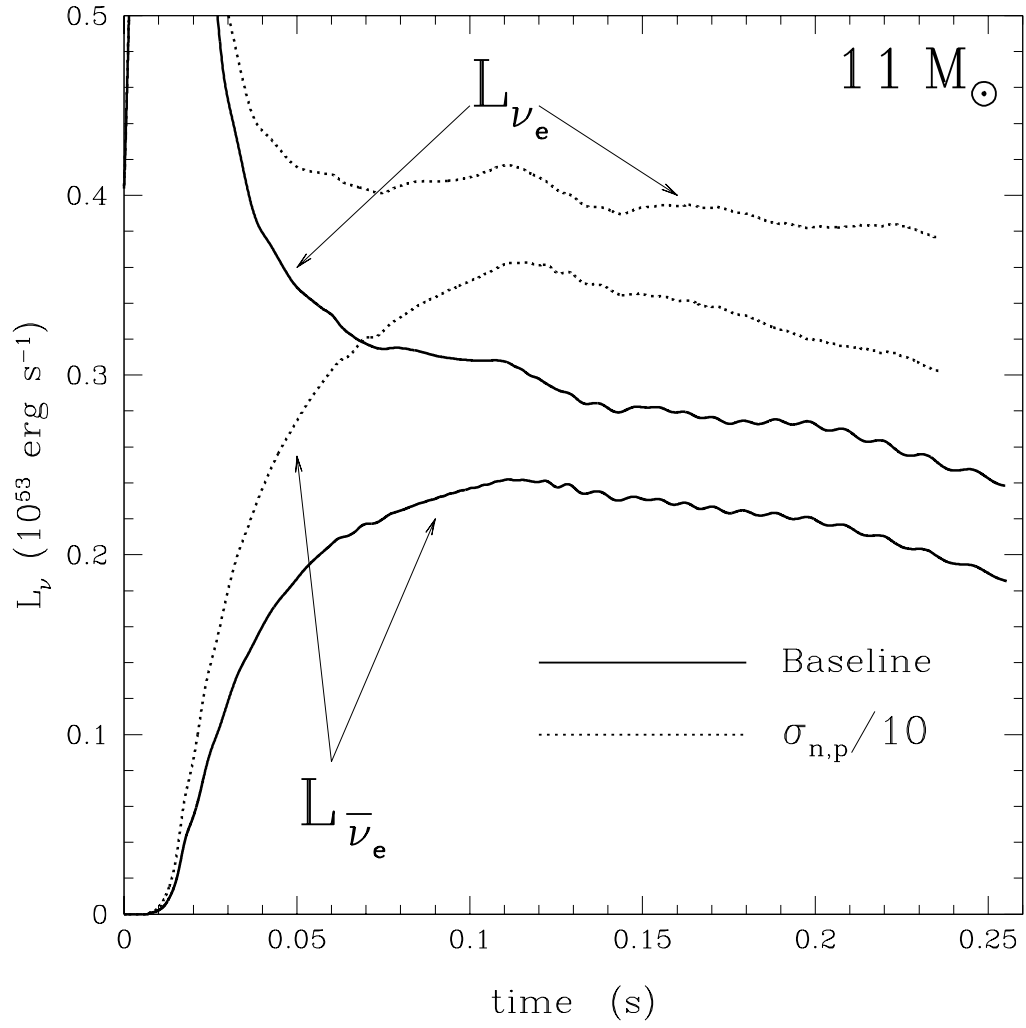
FIG. 15.— L_{ν_e} and $L_{\bar{\nu}_e}$ in erg s^{-1} at infinity as a function of time, for the fiducial model and for the model with artificially decreased neutral-current neutrino-neutron and neutrino-proton cross sections.
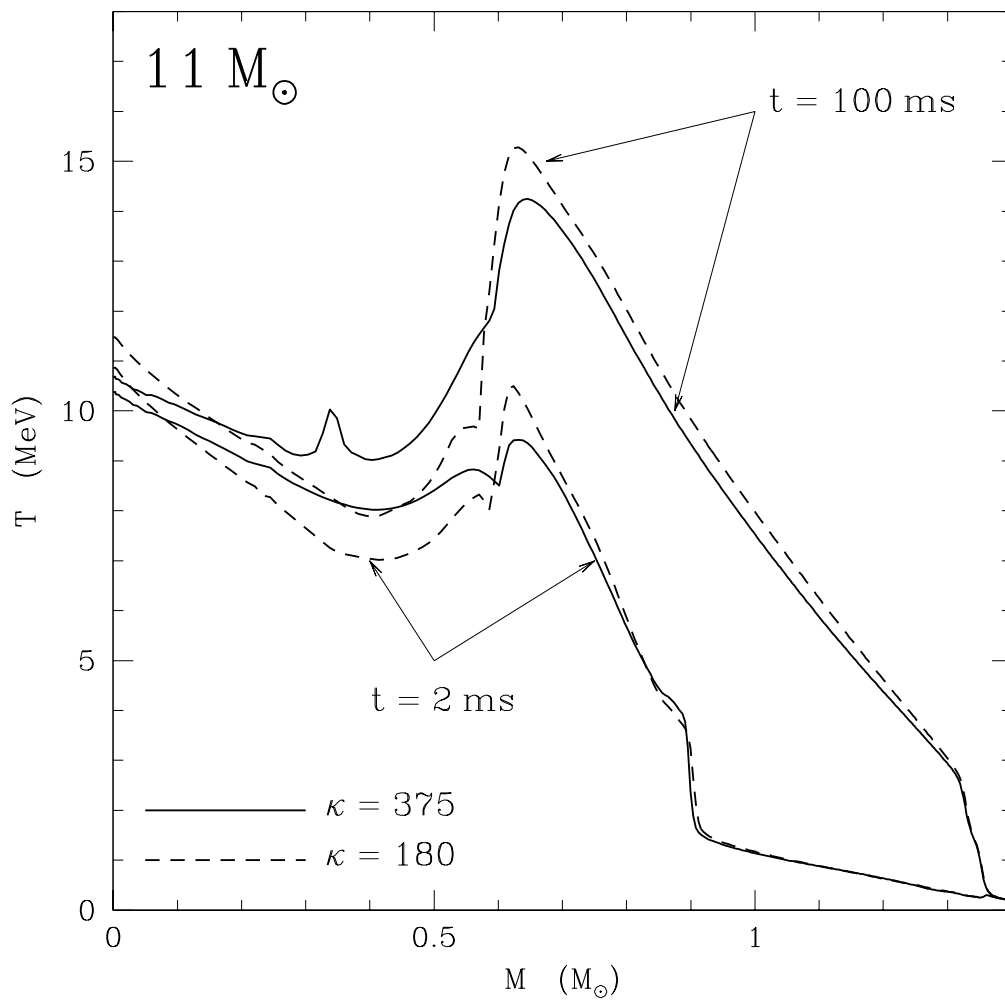
FIG. 16.— Temperature (T) in MeV as a function of mass coordinate in units of $M_\odot$ at two snapshots in time (~ 2 ms and ~ 100 ms post-bounce) for the 11 $M_\odot$ progenitor, using two different nuclear compressibilities, $\kappa = 180$ (dashed lines) and $\kappa = 375$ (solid lines).
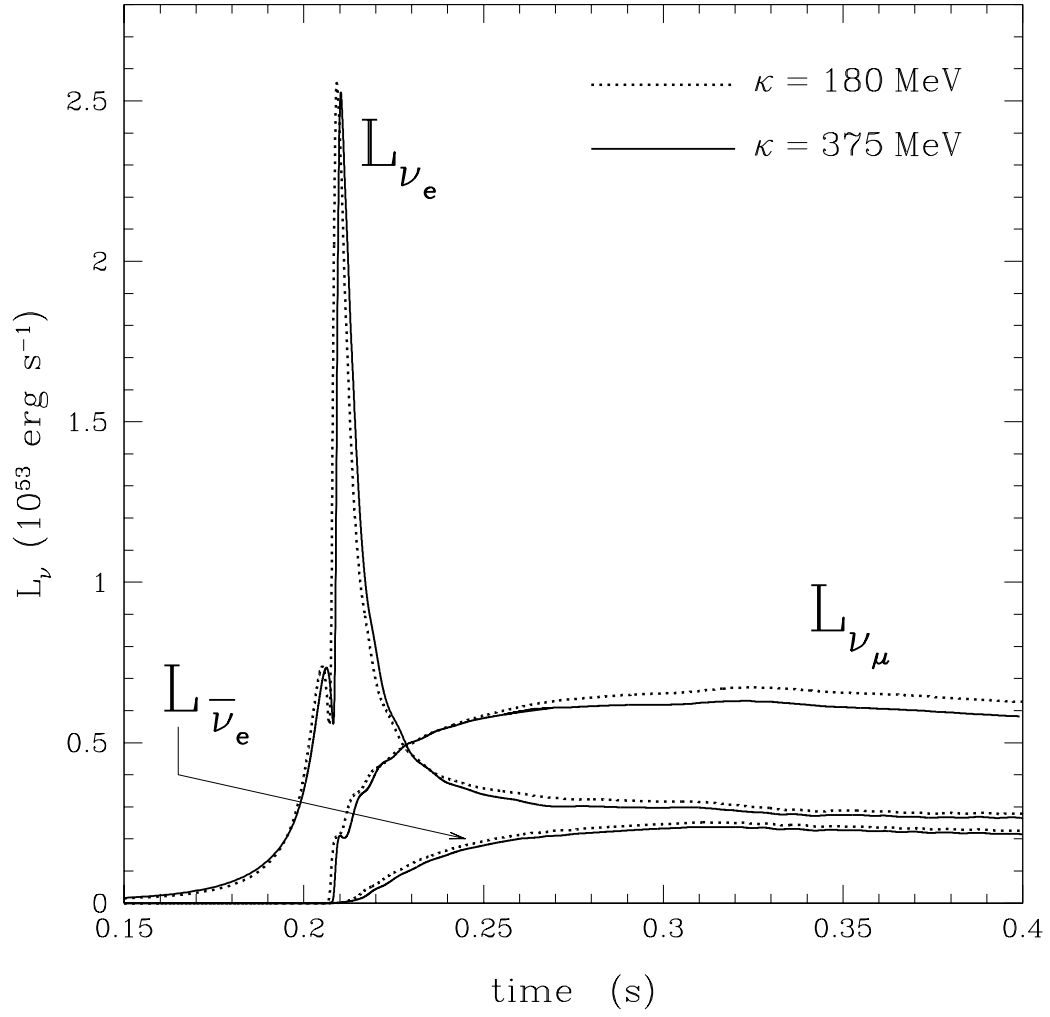
FIG. 17.— L_{ν_e}, $L_{\bar{\nu}_e}$, and L_{ν_μ} in units of 10^{53} erg s^{-1} at infinity for $\kappa = 180$ (dotted lines) and $\kappa = 375$ (solid lines).
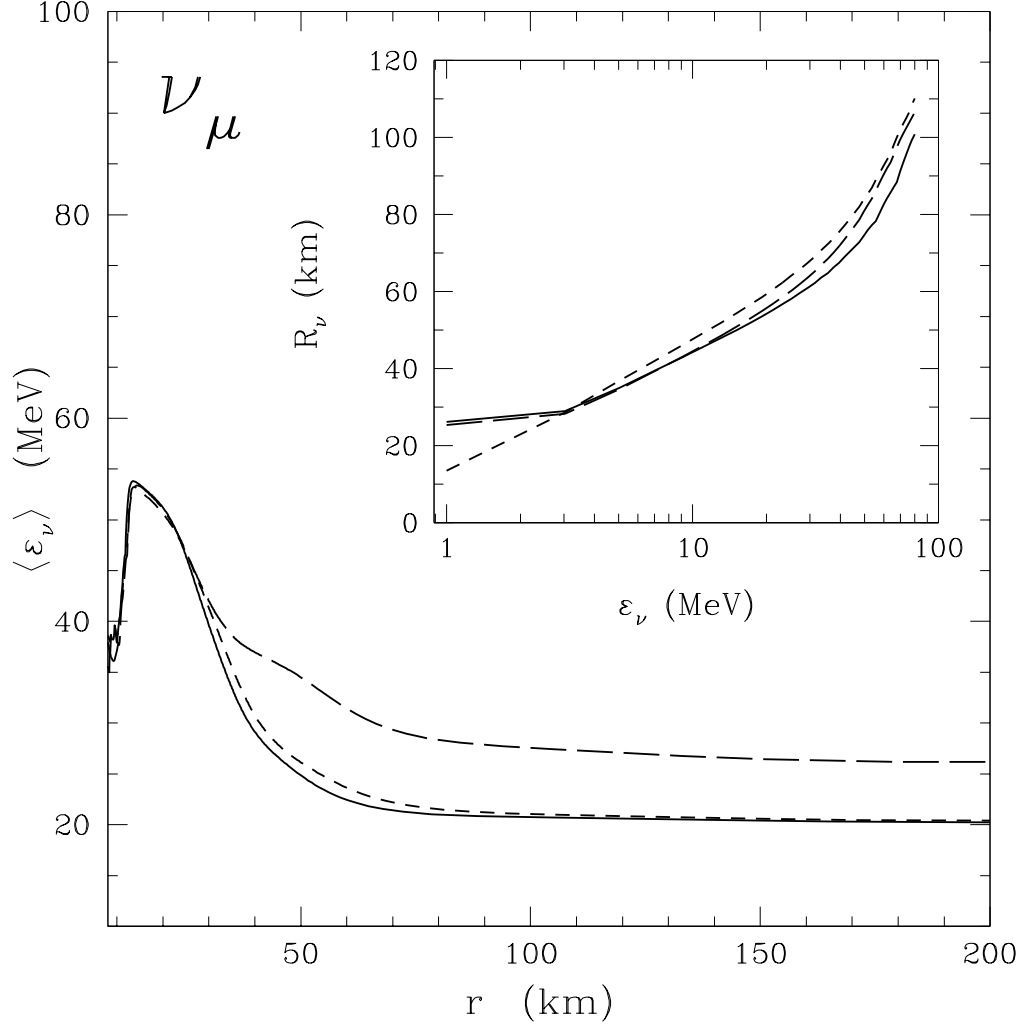
FIG. 18.— $\langle \varepsilon_{\nu_\mu} \rangle$ as a function of radius for $11\,M_\odot$ models with bremsstrahlung and inelastic neutrino-electron scattering (solid line), without bremsstrahlung and with inelastic neutrino-electron scattering (short dashed line), and with bremsstrahlung and without inelastic neutrino-electron scattering (long dashed line), approximately $220\,\mathrm{ms}$ after bounce. The inset shows the neutrinosphere R_{ν_μ}, defined by eq. (1) as a function of energy in the same models.
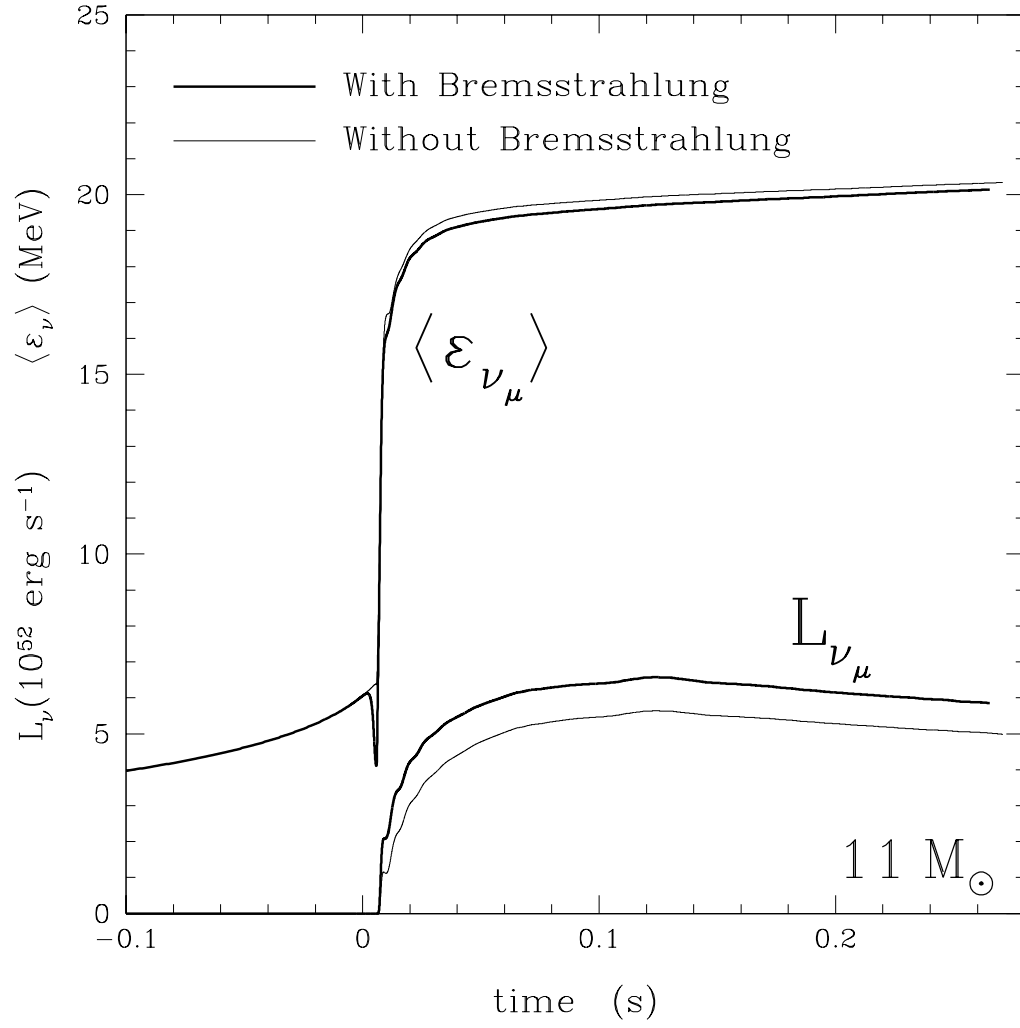
FIG. 19.— $\langle \varepsilon_{\nu_\mu} \rangle$ and L_{ν_μ} of the emergent spectrum at infinity as a function of time, for $11\,M_\odot$ models with (thick solid line) and without (thin solid line) nucleon-nucleon bremsstrahlung.
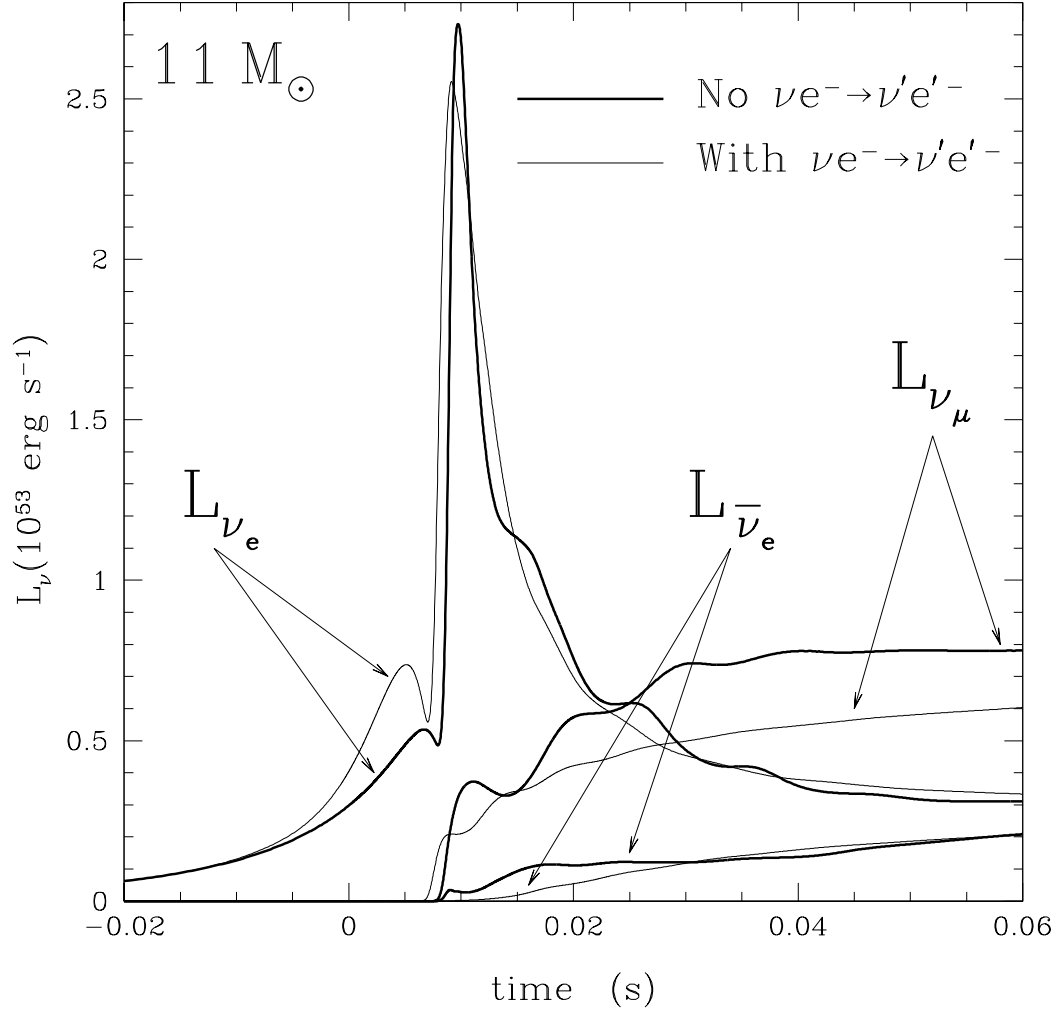
FIG. 20.— L_{ν_e}, $L_{\bar{\nu}_e}$, and L_{ν_μ} at infinity for the 11 M$_\odot$ progenitor with (thick solid lines) and without (thin solid lines) inelastic neutrino-electron scattering as described in Appendix §B.1.
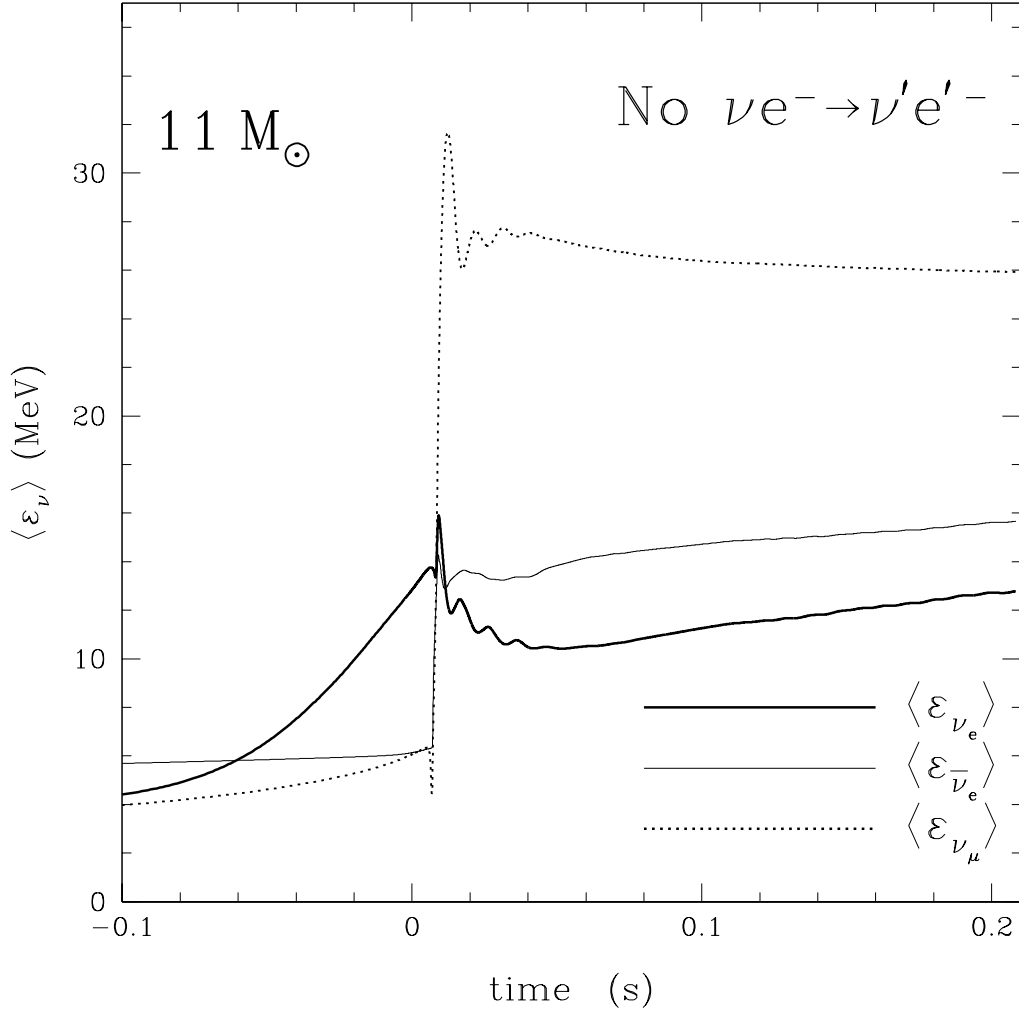
FIG. 21.— $\langle \varepsilon_{\nu_e} \rangle$ (thick solid line), $\langle \varepsilon_{\bar{\nu}_e} \rangle$ (thin solid line), and $\langle \varepsilon_{\nu_\mu} \rangle$ (dotted line) at infinity for the 11 $M_\odot$ progenitor without inelastic neutrino-electron scattering. Compare with Fig. 20, which shows the corresponding luminosities and Fig. 7, which shows the average energy evolution in our fiducial model (including inelastic neutrino-electron scattering).
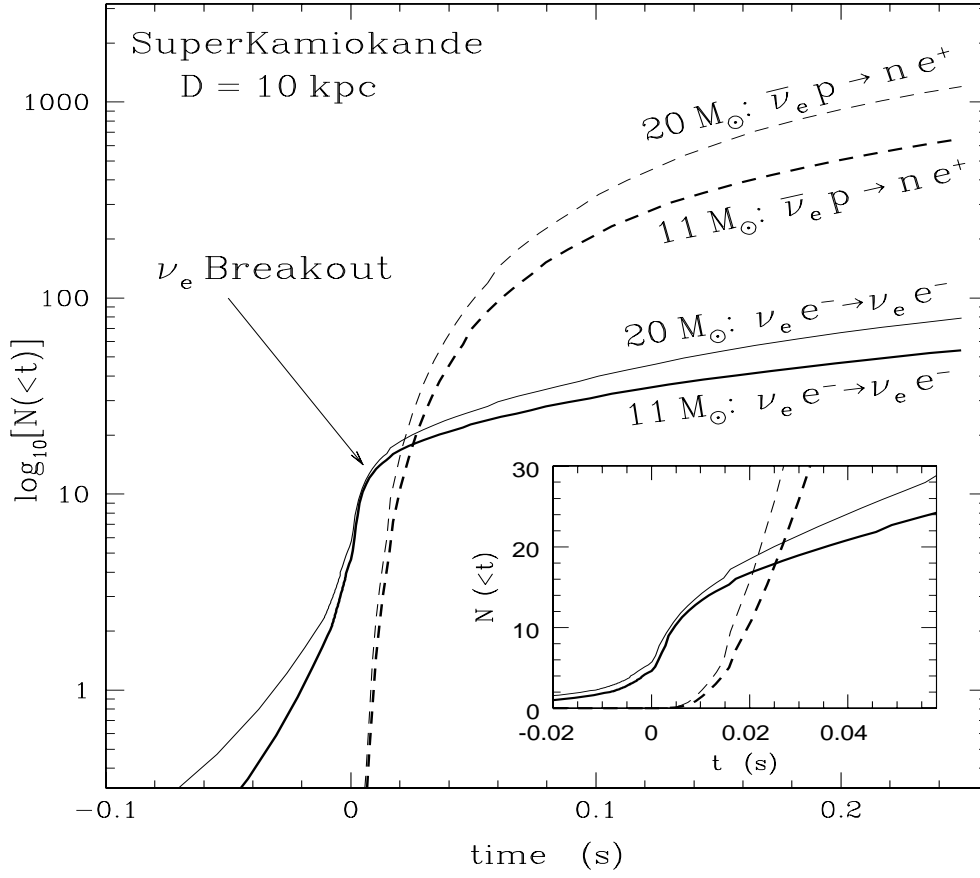
FIG. 22.— The integrated number of neutrino detection events ($\log_{10}[N(<t)]$) in SK for our $11\,\mathrm{M}_\odot$ (thick lines) and $20\,\mathrm{M}_\odot$ (thin lines) models via ν_e–electron scattering ($\nu_e e^- \rightarrow \nu_e e^-$, solid lines) and $\bar{\nu}_e$ capture on free protons ($\bar{\nu}_e p \rightarrow ne^+$, dashed lines) for supernovae at $10\,\mathrm{kpc}$. The inset is an expanded view of the ν_e breakout signal. Note that both models imply that SK should see a distinct and observable ν_e signature in the first $\sim 30\,\mathrm{ms}$. Nearly 20 ν_e events accumulate before being swamped by the dominant $\bar{\nu}_e$ signal. For clarity, we do not include the corresponding lines for the $15\,\mathrm{M}_\odot$ progenitor in this figure. The ν_e neutrino signal in the $15\,\mathrm{M}_\odot$ model is identical to that of the $11\,\mathrm{M}_\odot$ in the first 50 ms. The $\bar{\nu}_e$ event rate is slightly larger than that for the $11\,\mathrm{M}_\odot$ model; the $15\,\mathrm{M}_\odot$ model accumulates 680 events whereas the $11\,\mathrm{M}_\odot$ model yields 650 events in the 250 ms after bounce shown here.
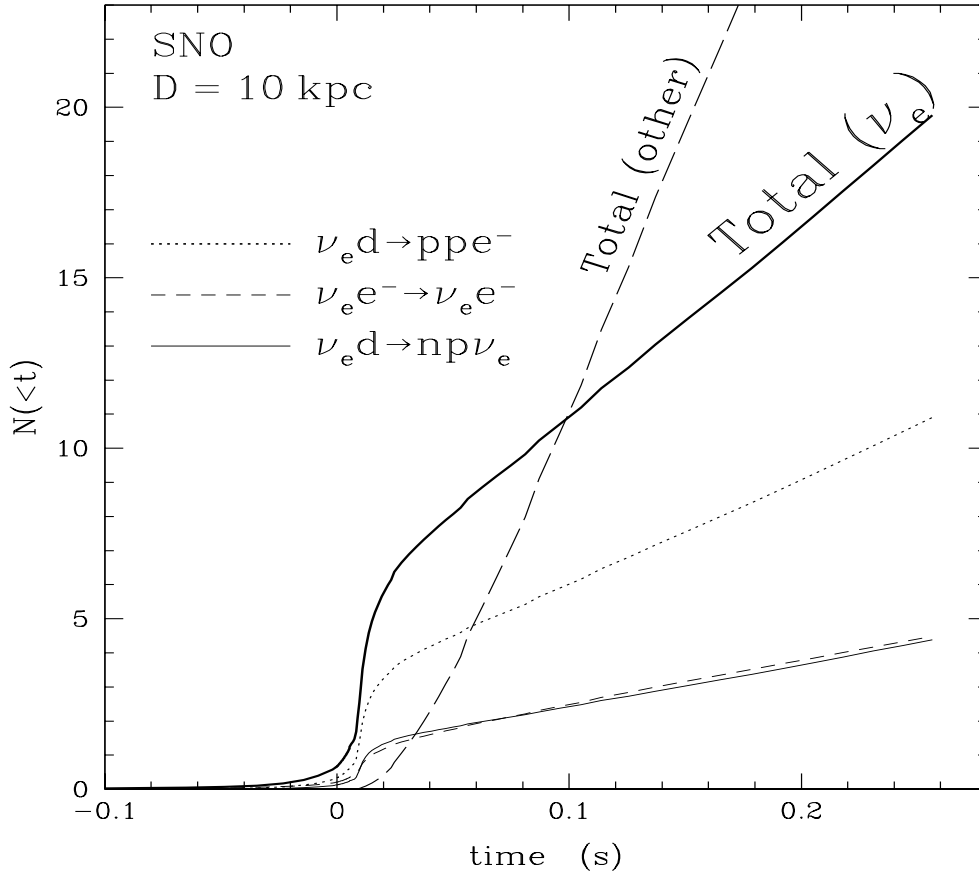
FIG. 23.— Integrated number of ν_e neutrinos detected in SNO for a supernova at 10 kpc as a function of time. The individual contributions to the detected signal via the $\nu_e d \rightarrow ppe^-$ (dotted line), $\nu_e d \rightarrow np\nu_e$ (solid line), and $\nu_e e^- \rightarrow \nu_e e^-$ (dashed line) processes are shown. The sum is the thick solid line. The sum of all other processes, including $\bar{\nu}_e d \rightarrow np\bar{\nu}_e$, $\bar{\nu}_e d \rightarrow nne^+$, $\bar{\nu}_e p \rightarrow ne^+$ in the light-water portion of the detector, as well as $\bar{\nu}_{\mu,\tau} d \rightarrow np\bar{\nu}_{\mu,\tau}$, $\nu_{\mu,\tau} d \rightarrow np\nu_{\mu,\tau}$, and $\bar{\nu}_e$-, $\nu_{\mu,\tau}$-, and $\bar{\nu}_{\mu,\tau}$-electron scattering throughout the entire detector volume, is shown as the long dashed line. This signal corresponds to our fiducial 11 $M_\odot$ core-collapse model.
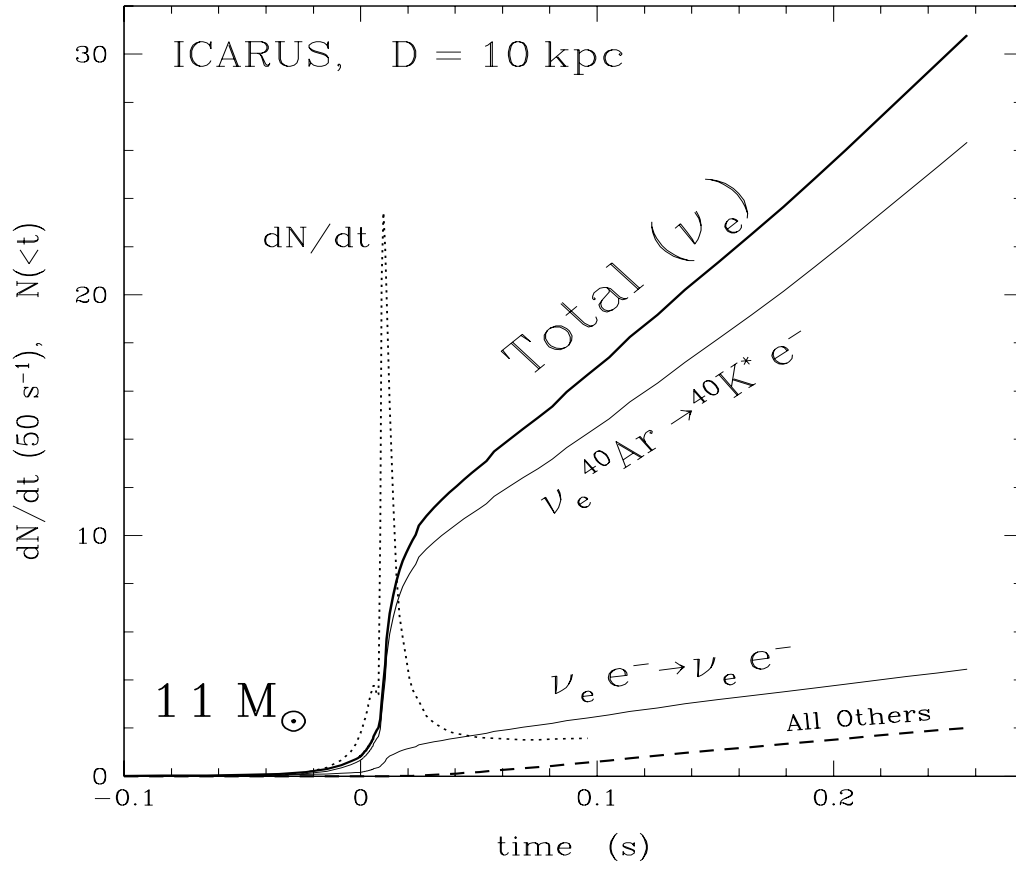
FIG. 24.— Integrated number of ν_e events as a function of time via absorption on Argon (labeled '$\nu_e \mathrm{Ar} \to \mathrm{K}^* + e^-$', solid line), including the Fermi and Gamow-Teller transitions to $^{40}\mathrm{K}^*$ (see §8.3), and via ν_e-electron scattering, labeled '$\nu_e e^- \to \nu_e e^-$' (solid line). The total number of ν_e neutrinos detected via these channels is the thick solid line. The thick dashed line (labeled 'All Others') shows the contribution to the total neutrino signal from $\bar{\nu}_e$, ν_μ, $\bar{\nu}_\mu$, ν_τ, and $\bar{\nu}_\tau$ neutrinos via scattering on free electrons. For reference, we also show the ν_e detection frequency (dN/dt, dotted line) during ν_e breakout and the first 100 ms after bounce.